To cite: M.F. Shahriar, A. Khanal, Fundamental investigation of reactive-convective transport: Implications for long-term carbon dioxide (CO2) sequestration, Int. J. Greenh. Gas Control. 127 (2023) 103916. https://doi.org/10.1016/j.ijggc.2023.103916.

Fundamental Investigation of Reactive-Convective Transport: Implications for Long-Term Carbon dioxide (CO_2) Sequestration

Md Fahim Shahriar[1], Aaditya Khanal[1*]

[1]The Jasper Department of Chemical Engineering, The University of Texas at Tyler

Corresponding author E-mail address: aadityakhanal@uttyler.edu

Abstract

The density-driven convection coupled with chemical reaction is the preferred mechanism for permanently storing CO_2 in saline aquifers. This study uses a 2D visual Hele-Shaw cell to evaluate and visualize the density-driven convection formed due to gravitational instabilities. The primary goal of the experiments is to understand the various mechanisms for the mass transfer of gaseous CO_2 into brine with different initial ionic concentrations and flow permeability. Moreover, the impact of CO_2 injection locations, reservoir dipping angle, and permeability heterogeneity is also investigated. We observed that the presence of salts resulted in earlier onset of convection and a larger convective finger wavelength than the case with no dissolved salts. Additionally, a higher lateral mixing between CO_2 fingers is observed when dipping is involved. The CO_2 dissolution, indicated by the area of the pH-depressed region, depends on the type and concentration of the ions present in the brine and is observed to be 0.38-0.77 times compared to when no salt is present. Although convective flow is slowed in the presence of salts, the diffusive flux is enhanced, as observed from both qualitative and quantitative results. Moreover, the reduced formation permeability, introduced by using a flow barrier, resulted in numerous regions not being swept by the dissolved CO_2, indicating an inefficient dissolution. We also investigated the effect of discrete high-conductivity fractures within the flow barriers, which showed an uneven vertical sweep and enhanced flow channeling. Lastly, the parameters regarding CO_2 leakage risk during storage are identified and discussed.

Keywords: CO_2 Sequestration; Convective dissolution; Reactive Dissolution; Rayleigh-Taylor instability; Heterogeneity; Permeability Contrast

To cite: M.F. Shahriar, A. Khanal, Fundamental investigation of reactive-convective transport: Implications for long-term carbon dioxide (CO2) sequestration, Int. J. Greenh. Gas Control. 127 (2023) 103916. https://doi.org/10.1016/j.ijggc.2023.103916.

1. Introduction

The atmospheric concentration of carbon dioxide (CO_2) in May 2021 was recorded as 419.5 parts per million (ppm), which is approximately 50% higher than at the beginning of the industrial revolution [1]. The growing concerns about CO_2 emissions have led to investigations of possible carbon capture and storage (CCS) methods. CO_2 geological storage in depleted oil reservoirs or saline aquifers is a preferred CCS method to capture emissions from large point sources [2]. CO_2 geological storage has four primary CO_2 trapping mechanisms: structural, residual, dissolution, and mineral trapping, as shown in Fig. 1 [3]. Capillary or residual trapping rate is the highest at the beginning of the CO_2 storage period; however, dissolution trapping becomes more dominant throughout time (**Fig. 1**). Dissolution trapping captures almost two-thirds of CO_2 injected in the storage volume [4–6]. Even though molecular diffusion of CO_2 in brine is slow, the rate of dissolution trapping is accelerated by other mechanisms, including density-driven convection or Rayleigh-Taylor instability, dispersion, and advection [7,8]. Several factors can affect the convective-dissolution phenomenon for different geological sites and, therefore, need to be considered for accurate CO_2 storage prediction. For example, density-driven convection is reduced for geological storages with lower vertical permeability, resulting in advection becoming the dominant force with increased transverse mixing [4,9]. Nevertheless, the effect of density-driven convection in CO_2 geological storage is significant, as it prevents CO_2 leakage by sinking CO_2 rather than rising to shallower formations [4]. Various studies have identified and extensively studied different aspects of the transport mechanisms during the density-driven convection or Rayleigh-Taylor instability, including diffusion period, convective period, and constant flux [10–15].

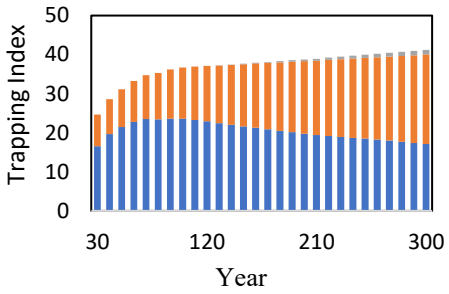

Figure 1. Fraction of CO_2 sequestered by residual trapping (blue), dissolution (orange), and mineralization (gray) (Modified from Khanal and Shahriar [3]). Dissolution is the primary storage mechanism especially with the passage of time.

Hele-Shaw cell, a simple structure usually formed by a narrow gap between two transparent flat plates, has been used in multiple experimental setups to visualize and mimic the Rayleigh-Taylor instability or Rayleigh convection (RC) formed during CO_2 storage in different geological structures [16–19]. Kneafsey and Pruess [20] conducted laboratory visualization studies and quantitative CO_2 absorption tests in transparent Hele-Shaw cells to investigate the dissolution-induced density-driven convection phenomenon. The quantitative measurements showed that the density-driven convection initiated faster than predicted. Backhaus et al. [21] studied the density-driven

convection for a lighter fluid (water) placed over a heavier fluid (propylene glycol). The initial instability and quasi-steady-state were explained by analyzing the convective time and velocity scales, finger width, and mass transport rate. The test was conducted at standard atmospheric conditions with a Rayleigh number (Ra) of 6000-90,000 [21]. Meanwhile, a smaller Ra range ($100 < Ra < 1700$) was adopted in the works of Slim et al. [22]. Potassium permanganate ($KMnO_4$) in water was used as an analog for CO_2 in brine at atmospheric conditions, describing the dissolution-driven convective behavior from the first contact up to 65% average saturation.

Developing scaling relationships, correlations, and models can provide important insight into the convection dissolution properties of CO_2 for different geological storage [2,23–26]. Motjaba et al. [23] developed two scaling relationships, one between Rayleigh and Sherwood numbers and the other between Rayleigh numbers and CO_2 convective flux for under 3.45 MPa and $182 < Ra < 20860$. Robust scaling relations between compensated flux and transition times between successive regimes in the system for different salt types (NaCl and $CaCl_2$) were examined by Mahmoodpour et al. [27]. The results showed that different salt types affect both the short and long-term dynamics of convective dissolution. Faisal et al. [24] obtained correlations between the Rayleigh number and the mass of total dissolved CO_2. Other useful scaling laws, including the onset of the convection, and wavelength of the initial convective instabilities, were also identified and discussed [5,28,29].

Different visualization techniques, including the Schlieren method, particle image velocimetry (PIV), laser-induced fluorescence (LIF), and interferometry method, have been adopted to observe the formation and growth of convective finger structures in Rayleigh convection [2,4,30,31]. Zhang et al. [2] presented a vortex model of CO_2 adsorption into the water to characterize the interfacial mass transfer coefficient for the continuous convective period. The study adopted particle image velocimetry (PIV) and laser-induced fluorescence (LIF) to calculate the Hele-Shaw cell's solute concentration distribution and instantaneous liquid velocity. Moreover, another recent work by Zhang et al. [32] used a different experimental setup using the UV-induced fluorescence method to investigate gas-liquid interphase mass transfer in a Hele-Shaw cell.

Mahmoodpour et al. [27] provided critical insight into visualizing the dissolution-driven convection at high-pressure conditions (up to 535.3 psi). They devised a novel Hele-Shaw apparatus withstanding high pressure and presented CO_2 dissolution-driven convective behavior in a confined brine-saturated porous medium. Tang et al. [4] designed a Hele-Shaw cell rated to 70 MPa and Ra of 346 to investigate the convection parameters, including critical

onset time of convection, dissolution rate, and gravitational instabilities. This study used the micro-schlieren technique to conduct the visual inspection. Pressure-volume-temperature (PVT) testing was conducted at 293.15 to 423.15 K and pressure ranging from 14 to 24 MPa.

The chemical composition of the CO_2 storage site also significantly affects the reactive transport of dissolved CO_2, as observed in the works of Thomas et al. [33]. Their work investigated the dissolution of CO_2 into an aqueous solution of bases MOH, where M^+ is an alkali metal cation. For bases MOH , the convection is enhanced for the counter-ion M^+ sequence of $Li^+ < Na^+ < K^+ < Cs^+$. The experimental investigation revealed that the base concentration in solution strongly impacts the nonlinear finger instability, where higher concentration leads to faster instability and shorter time for onset of convection. Furthermore, despite M^+ ions not actively participating in the geochemical reactions during the dissolution process, the nature of different M^+ ions varies in the instability development. Loodts et al. [34] observed the effect of pressure, temperature, and NaCl concentration on CO_2 dissolution properties. Their study suggested that increasing CO_2 pressure or reducing temperature or salt concentration leads to higher convective instability. However, temperature has a minimal effect on CO_2 dissolution properties, so controlling the temperature is not essential for the reproducibility of experimental studies [34]. Thomas et al. investigated the effect of salinity by the dissolution of gaseous CO_2 in pure water, Antarctic water, and 0.5-5 M NaCl dissolved in water [35]. The results showed that higher salt concentration delays the formation of instabilities, resulting in delayed onset of convection. Moreover, increased convection pattern wavelength and decreased fingers' velocity and the growth rate increased the salt concentration. Kim and Kim [36] derived and solved linear stability equations for the effect of chemical reactions in an initially quiescent vertical Hele-Shaw cell. Their nonlinear numerical simulation showed that chemical reactions enhance the diffusive flux; however, by retarding the onset of buoyancy-driven convective motion, convective flux is weakened.

Formation dip angle is another key factor of consideration for safely storing CO_2 on subsurface geological sites, as it significantly impacts spatial migration distribution during CO_2 dissolution [37–39]. For larger dip angles, the supercritical CO_2 phase could change to a gas phase during upward migration in the reservoir up-dip direction, where the reservoir formation temperature and hydrostatic pressure are lower [38]. As a result, reservoirs with higher dip angles have more chance of CO_2 leakage during geological storage. Jang et al. [37] simulated the effect of dip angle and salinity of CO_2 storage. For formation dip angles of 0°, 5°, and 10°, the migrated CO_2 distances were 60%,

73.3%, and 86.7%, respectively, compared to a 15° dip angle in the 200th year of CO_2 migration. Therefore, with a larger formation dip angle, there is a higher possibility of spatial CO_2 migration. They concluded that reservoirs with higher dip angles and salinity have low CO_2 geological storage safety. Wang et al. [38] observed similar effects of formation dip, where the total CO_2 storage amount is inversely proportional to the formation dip angle. The impact of dip angle is more prominent in storage reservoirs with higher porosity and permeability [38]. As Jing et al. [35] observed, higher salinity and high dip angle are not conducive to CO_2 geological storage. However, the effect of salinity is more significant than that of dip angle on the CO_2 liquid phase mass fraction.

During the injection of CO_2 in deep saline aquifers, the natural fractures present in the formation may propagate, or new fractures may be induced in the reservoir. The fracture networks in a hydrocarbon reservoir play a vital role in fluid transport from the pores to the wellbore as they are significantly more conductive than the matrix [40–43]. The same principle is applicable during the CO_2 sequestration operation, which makes it difficult to predict the movement of plumes during the injection of CO_2 in fractured porous media. The highly permeable conductive fracture networks can act as a pathway for fluid movement, potentially allowing CO_2 migration to neighboring aquifers or the surface through the cap rock [44,45]. Bond et al. [44] demonstrated improved CO_2 migration prediction by incorporating structural geological fractures in the model. Knowing the spatial distribution of fractures, their orientation, conductivity, and overall contribution to the effective permeability are desirable for geological sites whose permeability is controlled mainly by faults and fractures [45].

Despite the considerable investigative analyses on CO_2 dissolution-driven convection using the Hele-Shaw cell, some areas need further investigation. To the best of our knowledge, very few studies have considered the combined effect of dipping angle and varying salinity on CO_2 dissolution flow behavior. Since both the dipping angle and use of salts inhibit CO_2 dissolution, their combined effect needs to be further investigated. Moreover, the effect of varying CO_2 injection points needs further insight into quantitative analysis to make informed decisions about choosing optimal injection points. Additionally, despite the considerable theoretical model and experimental investigation on the effect of salinity in CO_2 dissolution, most of the work considers NaCl and ignores the presence of other salts. And to the best of our knowledge, the effect of fractures in heterogeneous media is yet to be presented. This experimental study critically investigates the effect of these factors to address this knowledge gap. Furthermore, this study discusses how the findings of this work can be translated into improving storage efficiency by providing

key insight into CO_2 convection dynamics. This study primarily investigates the effect of varying several parameters on the CO_2 mass transfer mechanisms in atmospheric conditions. However, since the actual reservoir conditions are at higher pressure and temperature, we provide a brief preliminary evaluation of the effect of high pressure and temperature in the discussions section and leave a more detailed investigation for future studies. Regardless, the fundamental qualitative investigation considered in this study still translates to actual reservoir conditions with similar non-dimensional numbers and thus can be accurately scaled without any loss of generality.

The remainder of the paper is organized as follows. **Section 2** provides the experimental setup, and **Section 3** presents the methods, image processing sequence, and a brief overview of the experiments considered. **Sections 4 and 5** present the qualitative visualization of CO_2 dissolution in homogeneous media without and with salt, respectively. **Section 6** considers the qualitative visualization of CO_2 dissolution in heterogeneous media. Additionally, the effect of fractures on CO_2 dissolution is also discussed. **Section 7** provides our results in terms of quantitative data. Lastly, **Section 8** is devoted to the discussion, and **Section 9** presents the main conclusions of this study.

2. Experimental Set-up

Experiments on atmospheric conditions (1.01 bar and 22° C) are performed in a Hele-Shaw cell composed of two transparent 0.5 in (12.9 mm) thick plexiglass separated by precision silicone shims with a thickness of 1 mm along the sidewalls. Although glass can have better thickness tolerance than plexiglass, this study considers plexiglass due to higher transparency, allowing enhanced clarity. The front plexiglass panel was drilled at the bottom of the cell and was fitted with a ball valve with a diameter of 0.25 in (6.35 mm). The internal cell dimensions were a length and height of 259 mm and 284 mm, respectively. The height (H) of the water column is 243 mm, as shown in **Fig. 2a.** This port was used to fill and drain the reactor of the experimental fluid.

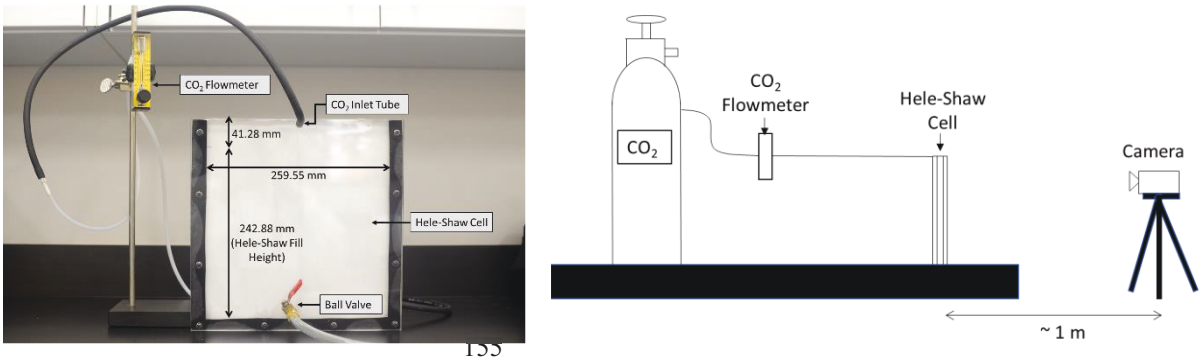

(a) (b)

Figure 2. (a) The Hele-Shaw cell with dimensions and (b) Schematic of the experimental setup

At the top, three holes at the center of the front plexiglass were drilled so that the CO_2 could be securely injected into the cell using an 18-gauge dispensing needle, as shown in **Fig. 2a**. A digital camera (Nikon D7000 with 50 mm lens) was focused on the cell to take pictures at 20 seconds intervals for 2.5 hours. We maintain a 4 cm distance from the injection point to the top of the water to avoid disturbing and introducing shear stress at the interface. The experiments used the same protocol to ensure a similar controlled environment. The schematic of the experimental setup is presented in **Fig. 2b.**

The flow of incompressible fluid in a Hele-Shaw is governed by the Navier-Stokes equation, coupled with the species conservation equation for cases with chemical reactions [24,46]. The conservation equations for mass, momentum, and species also implicitly consider the Boussinesq approximation, which assumes that the solute concentration affects the local density without causing an expansion or contraction of the fluid [47]. The permeability of the Hele-Shaw cell, k, with a cell aperture of b (for this study, 1 mm), can be obtained from the fundamental conservation laws as [48]:

$$k = \frac{b^2}{12} = \frac{0.001^2}{12} = 8.33 \times 10^{-8}\ \mathrm{m}^2 \quad (1)$$

As shown in **Eq. 1**, permeability is proportional to the square of the cell square; thus, slight variation in aperture can result in localized variation of permeability in the cell. As a result, the aperture variation must be checked to ensure acceptable thickness tolerance. We use the method proposed by Detwiler et al. [49] and Faisal et al. [24] to map the aperture variation of the Hele-Shaw used in this study. Using ImageJ, the light intensity transmitted through the cell is analyzed and normalized based on the average value. Then, the average cell aperture, calculated to be around 1.04

176 mm, is found by filling the cell with a known fluid volume. The fluctuations in cell aperture vary proportionally with
177 the normalized light intensity; therefore, by combining the normalized light intensity with average cell aperture, the
178 aperture variation in the cell up to the height of the water column is measured, shown in **Fig. 3.**

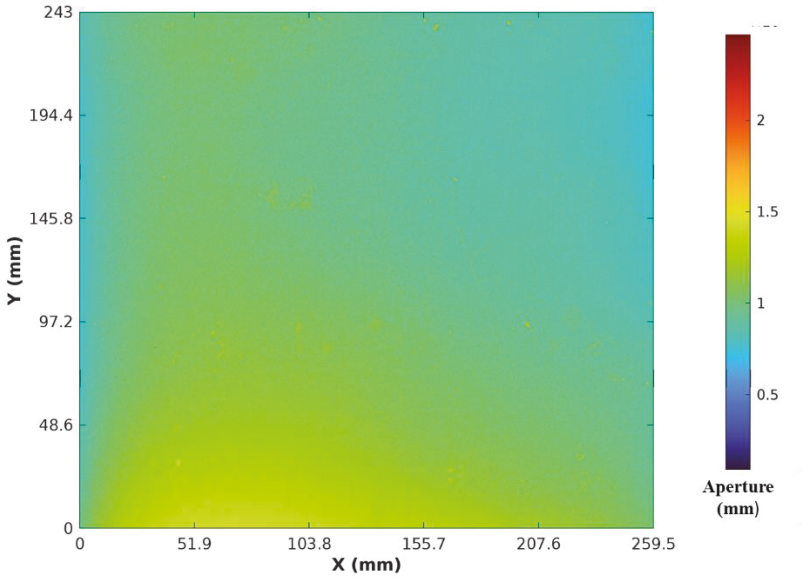

179

180 **Figure 3.** Aperture map resulting from the transmitted light analysis on the experimental 1 mm Hele-Shaw cell configuration

181 **Fig. 3** shows that the device used in this study is reasonably homogenous with negligible aperture variations, mainly
182 towards the bottom of the cell. The corresponding Rayleigh number (Ra), a dimensionless number characterizing the
183 system by expressing the ratio of free convection to diffusion, is calculated using the permeability (k) of the porous
184 medium and is represented as shown in **Eq. 2:**

191 $$\mathrm{Ra} = \frac{\Delta\rho g k H}{\mu\varphi\, D_{CO_2}} \tag{2}$$

185 Where g is the acceleration of gravity [m/s^2], H is the height of the water column [m], μ is the dynamic viscosity of
186 water [kg/m.s], D_{CO_2} is the molecular diffusion coefficient of CO_2 in water [m^2 /s], $\Delta\rho$ is the increase in density due
187 to CO_2 dissolution [kg/m^3], k is the permeability of the medium [m^2], and φ is porosity. For our experimental cases
188 without any heterogeneity, $\varphi = 1$. The aperture (1 mm) considered in this study is significantly small compared to the
189 height of the water column (243 mm), so the flow environment is mathematically analogous to the Darcy flow in
190 isotropic porous media. Therefore, the results presented in this study follow the same flow properties compared to

porous media [24,46]. However, additional porous material will introduce mechanical dispersion, in addition to convection, due to the flow path tortuosity and will require more in-depth analysis.[50].

For the heterogeneous cases, porosity, permeability, and corresponding Rayleigh number are calculated and presented in Section 3.2. We obtain a value of Ra = 41782 for the homogeneous base cases conducted in this study. It should be noted that the Rayleigh number will decrease slightly with an increase in salinity, as observed by Thomas et al. [35]. In their experiment, for salinities of 1M and 2M NaCl, the Rayleigh number decreased by 0.77% and 1.5%, respectively, compared to the Rayleigh number of the water system. We expect salinity to cause a similar decreasing pattern in Rayleigh number for cases with dissolved salts. The values for calculating the Rayleigh number were adopted from Faisal et al. [24], who used a bromocresol green pH indicator at a room temperature of 22 °C, similar to our experiments. As other theoretical studies and experimental investigations observed, for $Ra \geq 4\pi^2$, natural convection is the predominant flow [24,51]. All the experiments in this study meet that criterion for prevailing convective flow.

3. Experimental Procedure and Image Processing

The parameters considered for image analysis are the number of fingers formed, average finger length (mm), average wavelength (mm), area of pH depressed region (mm^2), and standard deviation of finger length (mm). Finger length is calculated as the vertical distance from the interface to the tip of the finger. In contrast, the average wavelength is the interface length divided by the number of fingers.

We followed the same image processing sequence adopted in the work of Kneafsey et al. [52]. Using ImageJ FIJI, we subtracted the initial condition (no CO_2) applied from all the images, resulting in images with less background noise in RGB format. Next, the RGB images were split into three color channels: red, green, and blue. The blue color channel containing mostly noise was discarded, while the two other channels were added, as shown in **Fig. 4**. Lastly, we inverted the grayscale lookup table changing dark to light, making the CO_2-dissolved pH-depressed regions darker. Additional image processing and noise removal were performed on some images for better clarity.

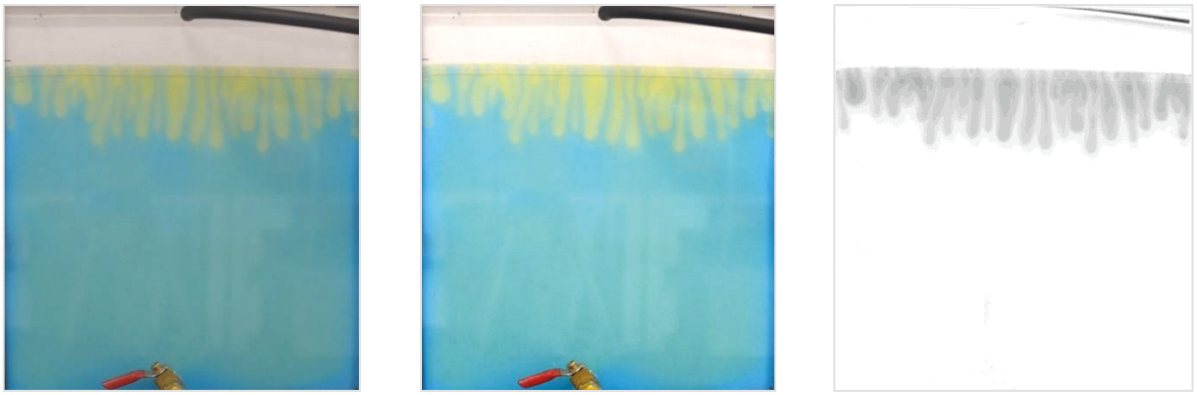

(a) Raw Image (b) Edited Image (c) Final Processed Image

Figure 4. Image Processing sequence showing (a) unedited image from the camera, (b) edited image with enhanced contrast, (c) grayscale image, which shows the final image used for analysis.

Before performing the experiments (**Table 1**), we conducted a repeatability test by comparing the qualitative and quantitative results of three runs for a test case where CO_2 was injected at the middle port of the Hele-Shaw cell filled with a solution prepared by mixing deionized, de-aired water with 0.0114% w/v Bromocresol Green (BCG). This solution is referred to as the *Control Fluid* (CF) in this study. BCG is a pH indicator that changes color from blue at a pH above 5.4 to yellow at a pH of around 3.9 [52]. The application of pH indicators is a widely accepted method for studying convective mixing [16,24,52,53]. Thomas et al. [54] indicated that the color indicator does not significantly affect the development of convective dynamics. Taheri et al. [55] reported no change in water's properties for a small amount of BCG. The solution in their experiment was prepared by mixing distilled deionized water with 0.025 wt. % BCG. Therefore, color-based pH indicators can be used when trying to quantify convective-dissolution properties [54,55]. The Hele-Shaw cell was filled at approximately 85% with 63 mL of CF. It is crucial to use a small flow rate so that the water interface at the top of the cell is not disturbed, which can add external perturbation to the interface and influence the viscous finger formation strictly due to gravitational instability. Therefore, we selected a flow rate of 0.59 L/min which showed no impact on the fluid interface, based on multiple runs with different flow rates. The selected flow rates resulted in a slow stream of bubbles when the CO_2 injection needle was placed in a beaker of water [24].

The qualitative results showing the convective pattern for the same time scale are presented in **Fig. 5,** which shows good repeatability for the finger size, number, and overall patterns when identical experimental conditions are

used for the runs. We also calculated the 95% confidence interval for various parameters that characterize the fluid flow presented later in the quantitative measurement section (**Section 7)**.

Run 1 Run 2 Run 3

Figure 5. Three runs for CO_2 introduced at 0.59 L/min to the left side of the cell at 85 min (CF, 1 mm aperture, vertically oriented flat glass)

The experimental investigations considered in our study can be divided into four cases, as presented in **Table 1.** In **Case A**, we consider the effect of the CO_2 injection point by varying the placement of the CO_2 injection point in the Hele-Shaw cell. Moreover, we also observe the effect of salinity by dissolving 1M $CaCl_2$ in the Control Fluid.

To observe the effect of initial cation concentration, we use $MgCl_2$ and $CaCl_2$ with varying concentrations in **Case B**, as shown in **Table 1.** The concentration of commonly dissolved solids in aquifer fluids can vary significantly based on the reservoir [56–60]. For example, the reported concentration of chloride ranges from 1.5 M (in Weyburn reservoir, Canada) to as high as 5.4 M (in Rose Run aquifer, Ohio) [57,59]. In comparison, several studies calculated Calcium concentration ranging from 0.05 to 0.9 M (2004 to 36072 ppm) and Magnesium concentration to be 0.02 M to 0.24 M (486 to 5834 ppm) [56–60]. The Mg^{++} and Ca^{++} cations are used in this study as they have received limited attention compared to numerous studies for Na+ cations. Furthermore, Mg^{++} and Ca^{++} cations form a significant fraction of the ions in worldwide saline aquifers [61]. This study aims to provide a comparative view of the impact of different salts; therefore, a uniform concentration of 1M and 2M is considered, which falls in the range of chloride concentration reported in different saline aquifers [57,59], as well as comparable to the concentration used in the work of Mahmoodpour et al. [62].

Additionally, we also introduce a slight dipping (≤ 1°) to mimic a dipping aquifer by raising the right side of the Hele-Shaw cell slightly higher than the left. When dipping is involved, the modified Ra is represented as shown in **Eq. 3** [52]**:**

$$\mathrm{Ra} = \frac{\Delta\rho g sin\theta k H}{\mu\varphi\, D_{CO_2}} \tag{3}$$

$Where, sin\theta$ is the parameter dictating the effect of gravity due to the dipping introduced. Thus, for a dipping angle of 1°, our corresponding Ra is 41775. It should be noted that, as we increase the dipping angle, the corresponding Ra can reduce significantly. For example, Kneafsey et al. [52] reduced their Ra value by a factor of 2 by orienting the cell 30º from the horizontal level.

Although **Cases A** and **B** consider homogeneity throughout the cell, CO_2 geological storage sites are heterogeneous. Barriers like calcite and shale layer are common forms of heterogeneity that can significantly dictate the density-driven natural convection mechanism [10]. Moreover, different configurations and geometries of the heterogeneities result in various convective flow directions and movements. Although several studies have introduced different heterogeneous patterns in the system [10,63,64] to observe and quantify the CO_2 dissolution-driven convection pattern, the effect of different salts in these heterogeneous systems is yet to be investigated. Therefore, in **Case C,** we add heterogeneities in the Hele-Shaw system by introducing regions with lower permeability values and observing the convection pattern change for solutions containing different salts. Moreover, despite the recognized importance of heterogeneous layers, the impact of fractures present in these heterogeneous formations has not been studied extensively [40,41]. Therefore, we created narrow spacing inside heterogeneous formations for Case D to mimic the convective flow through fractured regions. The CO_2 flow rate in all the experiments in **Case B, C,** and **D** is kept constant at a minimal flow rate of 0.59 L/min to prevent any disturbance at the water interface on top of the cell.

Table 1. The experiments considered in this study and the investigated parameters

Effect of Parameters Observed	Solution Used	CO_2 Injection Point	Case Number	Dipping Applied	Heterogeneous
CO_2 injection point and	*Control Fluid* (CF)[a]	Side	A1	No	No

Effect of salinity	CF	Middle	A2	No	No
	1 mole $CaCl_2$ dissolved in CF	Middle	A3	No	No
Dipping effect and presence of salt types with varying concentration	1 mole $CaCl_2$ dissolved in CF	Side	B1	Yes	No
	2 mole $CaCl_2$ dissolved in CF	Side	B2	Yes	No
	1 mole $MgCl_2$ dissolved in CF	Side	B3	Yes	No
	2 mole $MgCl_2$ dissolved in CF	Side	B4	Yes	No
Effect of Heterogeneity	CF	Side	C1	No	Yes
	1 mole $CaCl_2$ dissolved in CF	Side	C2	No	Yes
	1 mole $MgCl_2$ dissolved in CF	Side	C3	No	Yes
	1 mole NaCl dissolved in CF	Side	C4	No	Yes
Effect of Fracture	CF	Side	D1	No	Yes

[a]*Control Fluid* (CF) is prepared by mixing deionized 1 L of de-aired water with 0.0114% w/v BCG.

4. Qualitative Visualization for Homogeneous Case with No Salinity

4.1. CO_2 introduced to the side of the cell (Case – A1)

We introduce the gaseous CO_2 from the leftmost injection port for this case. The development of convection-driven fingering patterns is similar to what has been observed in previous studies [20,22,35,65]. CO_2 dissolution via diffusion was the only applicable mechanism at the initial stage of the visualization test, which we call the CO_2 induction phase. During the induction phase, there is a uniform change in pH near the gas-water interface, indicating the diffusion of CO_2, where the gaseous CO_2 dissolves in water to form aqueous CO_2 and forms equilibrium with carbonic acid, undergoing the following reactions [61]:

$$CO_2(g) \rightarrow CO_2(aq) \tag{4}$$

$$CO_2(aq) + H_2O \overset{K_1}{\rightleftarrows} H^+ + HCO_3^- \tag{5}$$

$$HCO_3^- \overset{K_2}{\rightleftarrows} H^+ + CO_3^{--} \tag{6}$$

$$H_2O \overset{K_3}{\rightleftarrows} H^+ + OH^- \tag{7}$$

287 During this period, the diffusive layer at the interface gradually expanded without any deformation or
288 instability. We observed the formation of fingers at around 135 ± 15 seconds, demonstrating the end of the induction
289 phase and onset of the convection process causing instability in the form of fingers, as shown in **Table 2**. We
290 considered the time frame for which the fingers are clearly visible; therefore, the actual onset of convection should be
291 slightly earlier since the earliest initiation of finger forming marks the onset of convective flow.

292 The fingers increased in width and depth as time progressed, traveling downwards vertically. The fingers
293 started merging as they grew in width, as evidenced by the decrease in the number of fingers and an increase in the
294 wavelength (please refer to **Section 7.1** for the quantitative measurement). Moreover, as time progressed, we observed
295 cell-scale convection, a phenomenon bringing fresh solution (solution not laden with CO_2) to the upper surface from
296 the center, as shown by small new fingers forming at the gas-water interface. The formation of distinctive new fingers
297 (also referred to as "nascent fingers") between established fingers can be seen as early as 27 minutes into the test. This
298 phase is identified as the reignition phase, which lasts until the end of the experiment, also observed in other studies
299 [22,35].

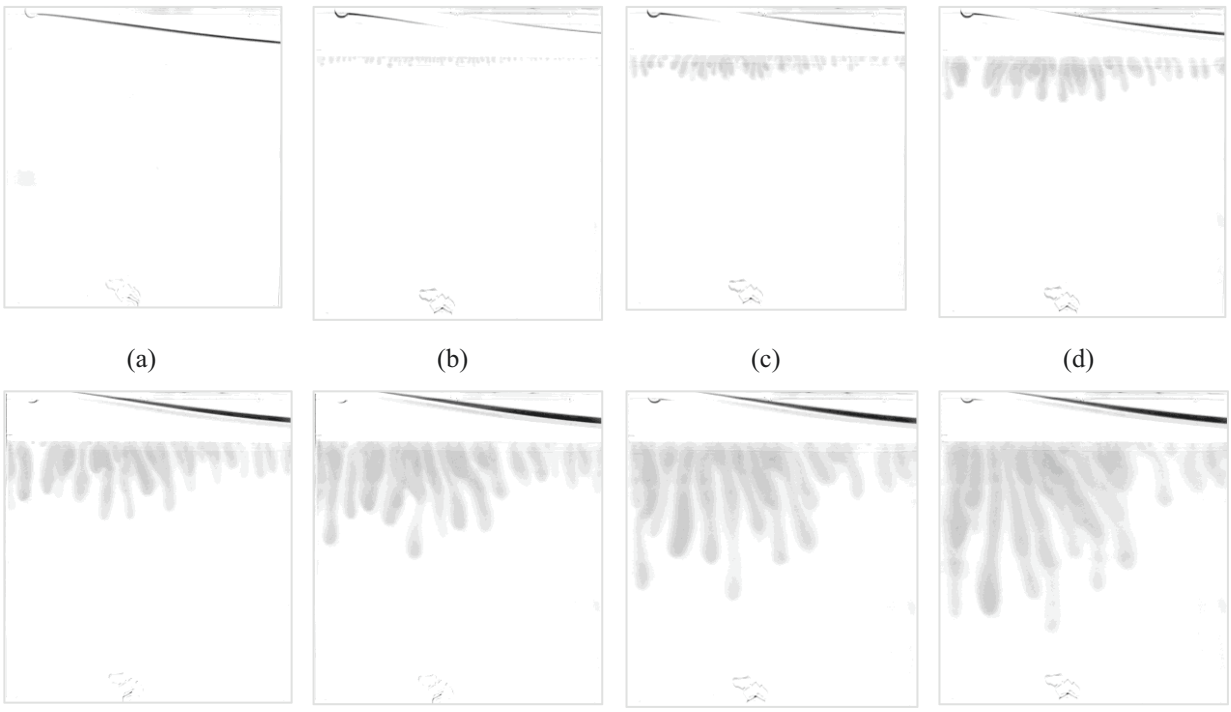

300

Figure 6. CO_2 introduced to the left side of the cell (CF, 1 mm aperture, vertically oriented flat glass) (a) Initial (no CO_2) (b) 9 minutes (c) 24 minutes (d) 36 minutes (e) 58 minutes (f) 85 minutes (g) 118 minutes (h) 154 minutes

The cell-scale convection also leads to the non-vertical movement (slight curve formed) made by the established fingers, which would otherwise move vertically due to density change and gravitational pull. The curved movement of the fingers can be observed as early as 9 minutes into the visualization test, shown in **Fig. 6 (b)**, which becomes more prominent as time progresses.

The whole area of the Hele-Shaw can be classified into two regions: active and inactive zones. The active zone can be referred to as the entire vertical region under the CO_2 injection point. In contrast, the region farther from the injection point can be identified as the inactive zone. As seen from **Fig. 6,** when CO_2 is injected into the left side of the cell, the area farther away from it, i.e., the inactive zone, has partially slowed finger formation. This difference can be attributed to the upward fluid flow due to cell-scale convection, which slows down the speed of the fingers. However, since the active zone has continuous CO_2 injection from the top, the effect of cell-scale convection in slowing down the finger flow is not as significant. Furthermore, due to the increasing difference in finger length between the active and inactive zones, we see an increase in the standard deviation of the finger length (refer to **Section 7.1** for a quantitative overview). Thus, injection near the boundary is clearly shown to have a different convective finger pattern from the injection at the middle of the cell, conducted in ours and several other studies [10,35,52].

4.2. CO_2 introduced to the middle of the cell (Case - A2)

To observe the effect of different injection points, as a slight variation of the first base **Case A1** we changed the injection point for **Case A2** (**Fig. 7**). We observed the CO_2 induction phase followed by a convection period, like the first base case. Furthermore, we also observed similar cell-scale convection during this visualization test.

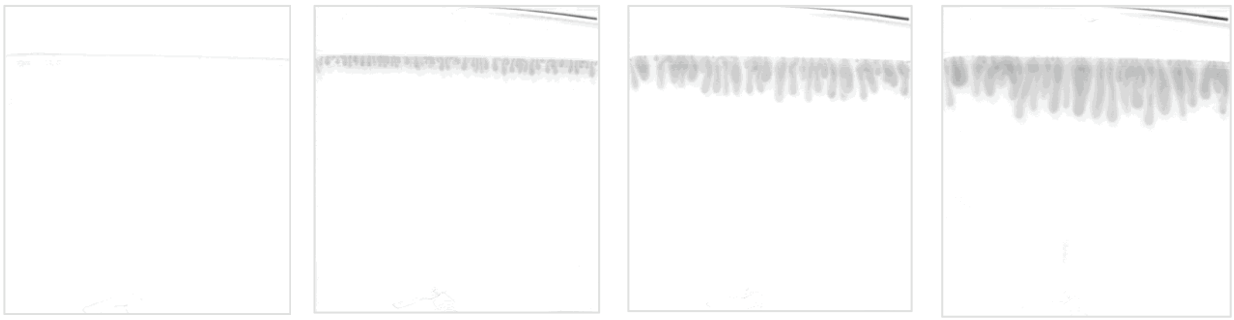

(a) (b) (c) (d)

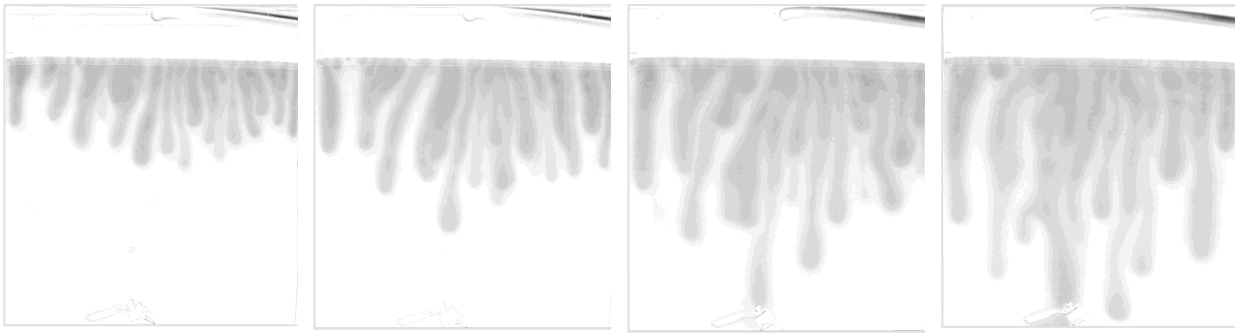

(e) (f) (g) (h)

Figure 7. CO_2 introduced to the center of the cell (CF, 1 mm aperture, vertically oriented flat glass) (a) Initial (no CO_2) (b) 9 minutes (c) 24 minutes (d) 36 minutes (e) 58 minutes (f) 85 minutes (g) 118 minutes (h) 154 minutes

Changing the CO_2 injection point also affected the layout of the active and inactive zones. For the first base case with CO_2 injection at the extreme left side of the cell, the inactive zone was much farther away at the right side of the cell. However, by injecting CO_2 in the middle of the Hele-Shaw cell, the inactive zones (the left and right sides of the cell) were relatively close to the active zone. The dissolution was symmetrical around the hypothetical vertical central line. At similar experimental conditions, Taheri et al. [10] observed the convection fingers at the side of the boundary cell moving faster than the middle of the cell. They named this phenomenon the 'side boundary effect,' which is not observable in our study. This can be due to the smaller gap width (0.25 mm) or larger Hele-Shaw cell dimensions (500 cm × 500 cm) adopted in their study.

As seen in **Fig. 6**, the fingers in the inactive zone had slower finger formation than those in the active zone, leading to a high standard deviation with time. However, **Fig. 7** shows that despite the inactive zone having slowed finger formation, it is not as significant as the previous base case **A1**, also evidenced by the smaller standard deviation in finger length compared to the previous test (see **Section 7.1**). This visualization proves that injection points can impact finger evolution. In the field scale, injection nearby vertical no-flow boundaries may impact the convective finger formations, so they should be considered during CO_2 geological storage.

Additionally, we observe the finger wavelength to be higher in **Case A3**, as the number of fingers formed is less in the presence of a salt. Furthermore, when comparing **Case A1** and **A2**, the wavelength at the onset of convection is higher when the injection point is at the side (**Case A1**). This difference can be attributed to the fact that during CO_2 injection at the side, the fingers at the inactive zone are not formed at the onset time of convection, thus reducing the

number of fingers formed, resulting in a higher wavelength. The slower finger growth in the inactive zone for **Case A1** is also observable in **Fig. 4 (b)**. We also considered the wavelength at 9 minutes, as shown in **Table 2. By that time,** all the fingers are visible and fully formed throughout the interface. At that period, the wavelength is almost similar for **Case A1**(4.55 mm) and **A2** (5.41 mm).

Table 2. Comparison and visual representation of the fingers at onset time of convection for Case A

Experiment Case	Solution Used	Picture at Onset Time of Convection[a]	Time (sec)[b]	Wavelength (mm)[c] At Onset of Convection	Wavelength (mm)[c] At 9 minutes
Case A1	CF		135 ± 15	5.3	4.55
Case A2	CF		135 ± 15	3.56	5.41
Case A3	1 mole $CaCl_2$ dissolved in CF	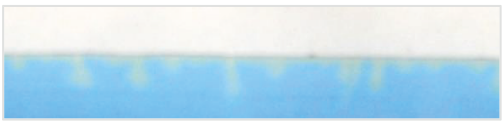	105± 15	6.33	6.83

[a]*The region under the injection point is cropped and edited for better visibility*

[b]*For the onset time of convection, we consider the time for which the fingers are clearly visible*

[c] *Wavelength is the ratio of the length of interface and the number of fingers for that particular interval*

Onset time of convection, or the time at which the host phase experiences instability in the dissolution-driven convection flow, is an important aspect of safe CO_2 storage and risk assessment. A shorter onset time of convection is desired, as convection enhances the mixing of CO_2 in brine, allowing faster CO_2 movement away from the caprock downwards in the brine [35]. It should be noted that the onset time of convection is defined differently by several studies [24,28]. This study considers the qualitative onset time of convection, referring to the time point when finger formation is clearly observable, as provided in **Table 2**, with the corresponding finger wavelength at the onset of convection. **Table 2** shows that the injection point does not impact the onset time of convection, which is observed to

be around 135 seconds (**Case A1** and **A2)**. However**,** the convection initiates earlier in the presence of a salt ($CaCl_2$). This result agrees with Jiang et al. [66], who observed the onset time to be 130 s for pure water, 100 s for 0.25 wt.% saline water, and 20 s for 1.00 wt.% saline water. Several other studies reported the onset of convection as the time when the mass flux deviates from pure diffusion [11,20,22]. Using stability analysis theory, the minimum theoretical onset time of convection, provided by Lindeberg and Wessel-Berg [67], is represented in **Eq. 8**.

$$t_c = c1\left(\frac{\mu\varphi\sqrt{D_{CO_2}}}{\Delta\rho g k}\right)^2 \tag{8}$$

For Ra>>40, the horizontal wavelength which most easily causes instability is presented in **Eq. 9**.

$$\lambda_c = c2\left(\frac{\mu\varphi\pi D_{CO_2}}{\Delta\rho g k}\right) \tag{9}$$

Different studies have reported the values of c1 and c2 differently. Based on numerical stability analysis, the minimum theoretical value is reported as c1 = 48.7 and c2 = 96.23 [67]. Using Ra values ranging from 40 to 370 and at 4 MPa, Kneafsey and Pruess experimentally evaluated c1 of 48 to 177 [20]. On the other hand, Pau et al. [28] reported a much higher range of c1 from 1796 to 3670. Similarly, Pruess and Zhang et al. [68] reported a c1 value of 1155.6 and 1411.5 in their study. In our study, the c1 value was obtained to be 5770. Furthermore, the value of c2 ranged from 195 to 290. Notably, the critical wavelength and onset of convection predicted by linear stability analysis are usually smaller than the experimental value. The discrepancy can be attributed to the fact that the very onset of fingers is differently defined, and the fingers may not be detectable before they are visually observable in experimental studies [11]

5. Qualitative Visualization for Homogeneous Case with Varying Salinity

5.1. 1 mole $CaCl_2$ dissolved in Control Fluid – CO_2 introduced to the middle of the cell (Case A3)

The presence of salt stabilizes the convective dissolution of CO_2, as predicted in the theoretical work by Loodts et al. [34] and also shown experimentally in Thomas et al. [35]. By adding salt or increasing salt concentration, the solubility of CO_2 decreases, consequently reducing the density gradient between the fresh solution and the CO_2 mixed solution. Moreover, the system is also stabilized by the increasing viscosity of the solution caused by higher concentrations of salt [34,69]. Since the formation and development of convection-driven flow depends on density-driven gravitational instabilities, the convection process is slowed down in a stable system [34,35,52]. This is also evident from our visualization tests, as seen in **Fig. 8,** and our quantitative measurements (**Section 7**).

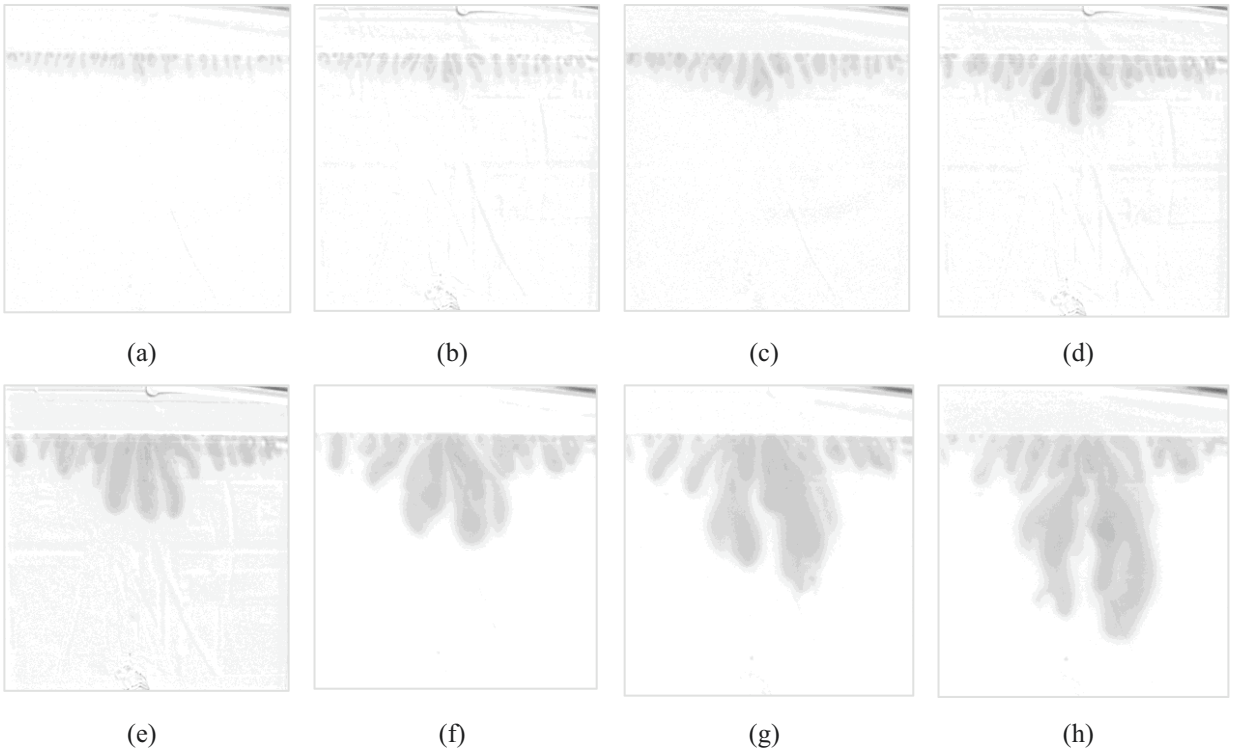

Figure 8. CO_2 introduced to the center of the cell (1 mole $CaCl_2$ dissolved in CF- 1 mm aperture, vertically oriented flat glass) (a) 9 minutes (b) 15 minutes (c) 24 minutes (d) 36 minutes (e) 58 minutes (f) 85 minutes (g) 118 minutes (h) 154 minutes

Although the symmetry around the hypothetical vertical line is maintained, the presence of $CaCl_2$ severely hindered the finger growth rate in the inactive zones, resulting in a large standard deviation throughout the test, as seen in **Fig. 8**. Moreover, we also observed a reduction in the number of fingers formed, the maximum being 38 at 540 seconds. Unlike the previous base cases where fingers were formed close to one another, the fingers formed in this case were placed at a minimal distance from each other, as observed in **Fig. 8 (b)**. The visualization tests show the importance of knowing the constituents and their composition level for a saline aquifer beforehand to predict the expected CO_2 storage behavior.

The pore fluid in saline aquifers contains different compositions of ionic solutions, with common components including Calcium, Magnesium, Potassium, Iron, Chloride, Sulphate, etc., which leads us to investigate the CO_2 dissolution-driven convection phenomenon in $CaCl_2$ and $MgCl_2$. [61,70]. The presence of different minerals in sandstone formations has a direct effect on CO_2 mineral trapping and also plays a role in altering reservoir transport properties [61,71]. For example, Anorthite ($CaAl_2Si_2O_8$), a common Ca-bearing feldspar, in sedimentary rock aids in

faster reaction kinetics and higher CO_2 reactivity, thus enhancing the reservoir rock porosity as well [71]. We refer our readers to the review of Silva et al. [61] for the detailed geochemical aspects of CO_2 sequestration in deep saline aquifers.

As observed by Liu et al. [70], in the presence of salt ions like NaCl, $CaCl_2$, or $MgCl_2$ in pore fluid, water molecules bind with the "solvates," leaving less water for CO_2 dissolution. The precipitation reactions for Ca^{2+} and Mg^{2+} ions result in the formation of Calcite ($CaCO_3$) and Magnesite ($MgCO_3$), respectively, as shown in **Equations 10** and **11** [61].

$$Ca^{2+}(aq) + CO_3^{2-}(aq) \rightarrow CaCO_3(s) \quad (10)$$

$$Mg^{2+}(aq) + CO_3^{2-}(aq) \rightarrow MgCO_3(s) \quad (11)$$

Even though most theoretical benchmarks and simulation studies consider ideally horizontal geological storage sites, it is exceedingly rare in real-life scenarios. Most of the storage sites have a formation dip angle, thus making it another key factor of consideration for safely storing CO_2 on subsurface geological sites [37–39]. To visualize the effect of different salts with varying concentrations with a minimal dipping angle, we introduced CO_2 to the left side of the cell. The right side of the Hele-Shaw cell was placed about 1° higher than the left side for the experiments in **Case B**. This allows us to inspect the CO_2 convective dissolution in regions farther from the injection point and the effect of dipping. Furthermore, the qualitative findings from the experiments allow investigation of the changes due to different salts in saline aquifers. We prepare the solution by dissolving salt with different concentrations in the CF for the visualization tests.

5.2. $CaCl_2$ dissolved in Base Case Fluid – CO_2 introduced to the side of the cell (Case B1 and Case B2)

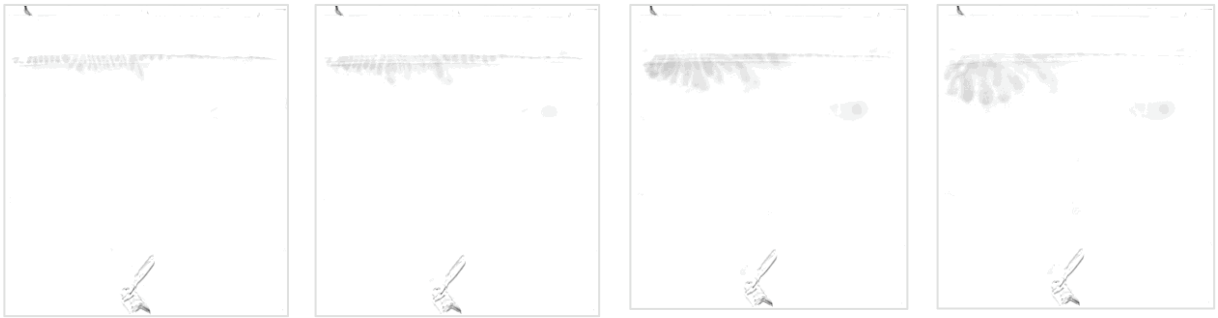

(a) (b) (c) (d)

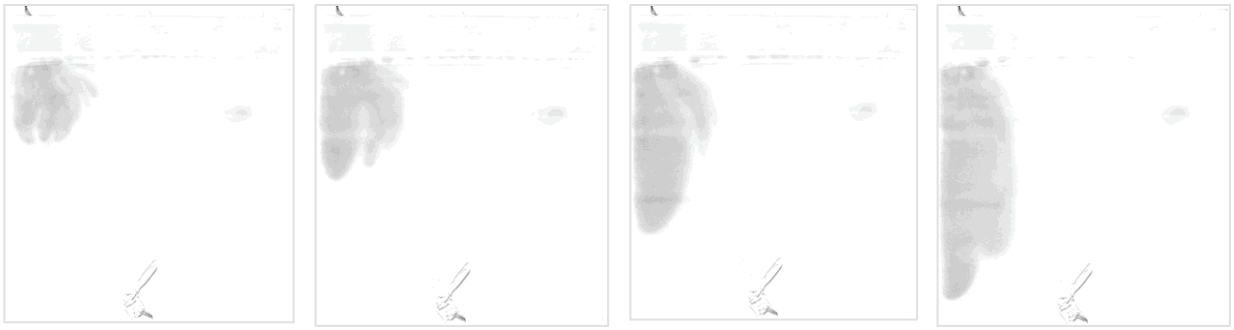

(e) (f) (g) (h)

420

421 **Figure 9**. CO_2 introduced to the side of the cell at 0.59 L/min(1 mole $CaCl_2$ dissolved in CF- 1 mm aperture, vertically oriented flat glass, **Case**

422 **B1**) (a) 9 minutes (b) 15 minutes (c) 24 minutes (d) 36 minutes (e) 58 minutes (f) 85 minutes (g) 118 minutes (h) 154

423 minutes

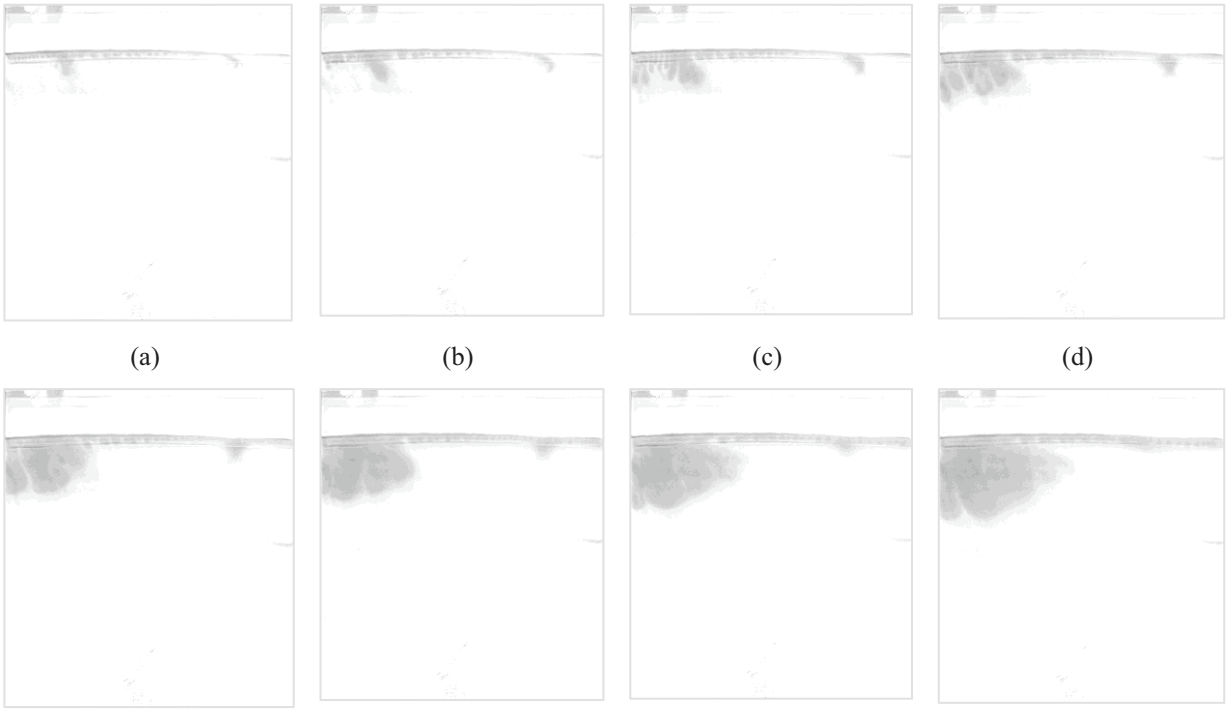

(a) (b) (c) (d)

(e) (f) (g) (h)

424

425 **Figure 10**. CO_2 introduced to the side of the cell at 0.59 L/min (2 mole $CaCl_2$ dissolved in CF- 1 mm aperture, vertically oriented flat glass,

426 **Case B2**) (a) 9 minutes (b) 15 minutes (c) 24 minutes (d) 36 minutes (e) 58 minutes (f) 85 minutes (g) 118 minutes (h)

427 154 minutes

The effect of the CO_2 injection point near the boundary and the dipping angle is observable by comparing **Case A3**, **Case B1, and B2.** For **Case B1 and B2**, the fingers formed near the boundary can't move freely due to restricted space and merge with the nearby fingers, resulting in bigger oval-shaped finger formations, as seen in **Fig. 9 and 10**. Moreover, due to the dipping angle, with the right side of the cell being placed higher, the finger formation on the right side is severely impacted. The finger formed on the right side moves laterally and mixes with the left side fingers, aiding in the oval-shaped finger formation. The formation of nascent-fingers is observed, and the cycle of lateral finger movement and finger-merging continues throughout the experiment. Whereas, without any boundary effect, as represented by CO_2 injection in the middle (**Case A3**), the coalesced fingers in the active zones protrude in different directions rather than forming a large oval-shaped finger formation.

The effect of increased salt concentration is visualized in **Case B2,** which has a higher $CaCl_2$ concentration, resulting in a lower CO_2 solubility. Moreover, the formation and development of convective-driven flow are slowed in this case, as shown in **Fig. 8**. The vertically downward finger movement is slowed significantly, alluding to the reduced impact of gravity-driven convectional instabilities.

5.3. Effect of $MgCl_2$ with different concentration (Case B3 and Case B4)

Fig. 11 and 12 show that **t**he solution with $MgCl_2$ has higher CO2 convective flow than CaCl2, which is evident from a higher pH depressed area (indicating dissolved CO_2) in the pictures. The CO_2 dissolved area indicated by the pH-depressed region follows the order of $CaCl_2$ 2M solution < $MgCl_2$ 2M solution < $CaCl_2$ 1M solution < $MgCl_2$ 1M solution. Detailed quantitative analysis of the pH depressed zone for the salts are provided in **Section 8.** Besides that, we observe the same effect of dipping angle on CO_2 dissolution in the presence of $MgCl_2$. Lateral mixing is observed in both lower and higher concentrations of $MgCl_2$. However, the vertical movement of the finger is considerably slowed down at 2M $MgCl_2$ solution, as shown in **Fig. 12**.

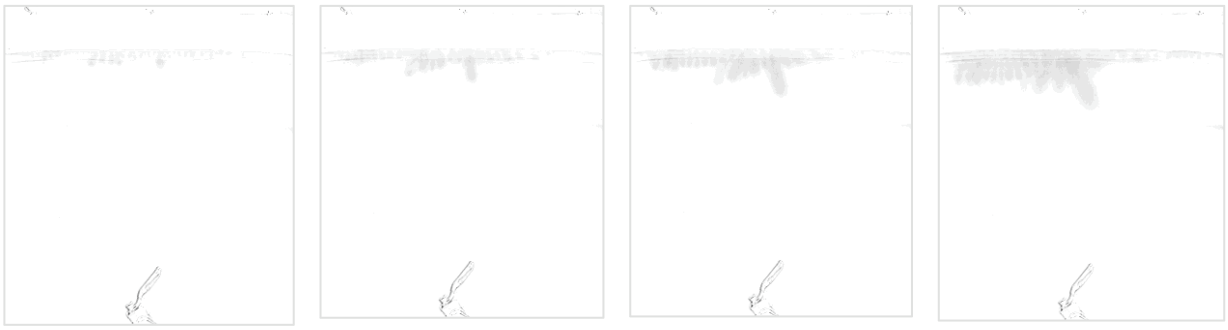

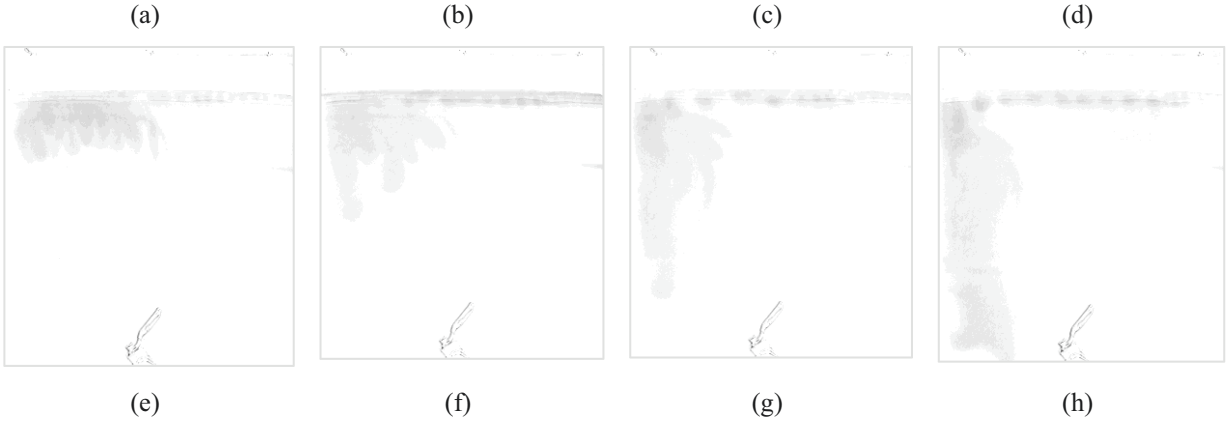

449

450 **Figure 11**. CO_2 introduced to the side of the cell at 0.59 L/min (1 mole $MgCl_2$ dissolved in CF- 1 mm aperture, vertically oriented flat glass,

451 **Case B3**) (a) 9 minutes (b) 15 minutes (c) 24 minutes (d) 36 minutes (e) 58 minutes (f) 85 minutes (g) 118 minutes (h)

452 154 minutes

453

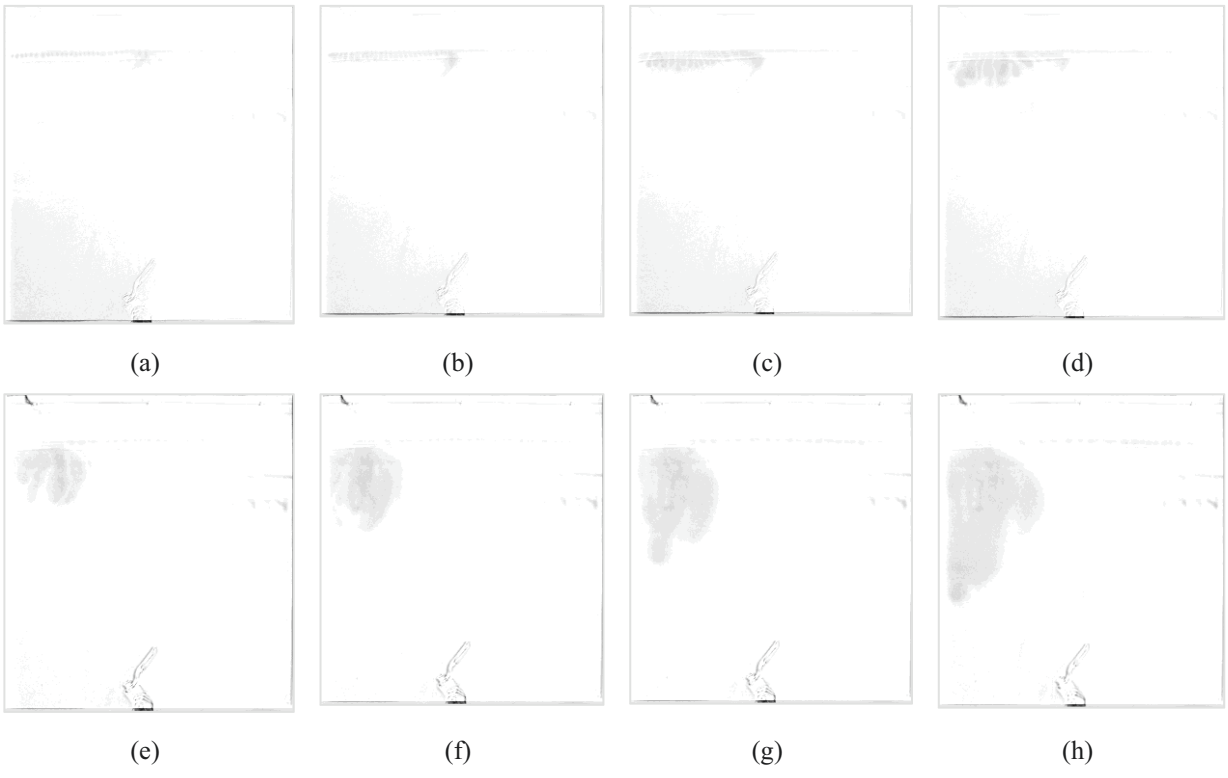

454

Figure 12. CO_2 introduced to the side of the cell at 0.59 L/min (2 mole $MgCl_2$ dissolved in CF- 1 mm aperture, vertically oriented flat glass, **Case B4**) (a) 9 minutes (b) 15 minutes (c) 24 minutes (d) 36 minutes (e) 58 minutes (f) 85 minutes (g) 118 minutes (h) 154 minutes

6. Qualitative Visualization for Effect of Permeability Heterogeneity (Case C and D)

All the storage sites have some form of vertical and horizontal permeability heterogeneities introduced by calcite layers or shales, which play a major role in dictating fluid flow [10,64]. Different convective-flow patterns (gravity fingering, channeling, or dispersion) can be observed based on the heterogeneity medium. Depending on the heterogeneity parameters, the average CO_2 mass flux at the top boundary can reach different constant values after decreasing at the initial stage and then increasing, as shown by Ranganathan et al. [72].

In this section, we investigate the effect of heterogeneities on convective behavior by setting up multiple 0.05 mm thick graphite strips (99.5% graphite flexible sheet) inside the Hele-Shaw cell, thus reducing the aperture to 0.05 mm for these regions. The length and height of these graphite strips are 50 mm and 12.7 mm, respectively. Furthermore, to prevent any airborne hydrocarbon contamination, the cell was cleaned thoroughly using distilled water, and the graphite strips were replaced with new ones prior to conducting the experiments. The graphite strips were selected for ease of removal and adhesion to the cell walls. Although silicone shims were used for setting up the Hele-Shaw, they merely act as a boundary and do not affect the flow properties inside the cell. Therefore, the surface properties (e.g., wettability, interfacial tension, etc.) remain the same for all the experiments where the effect of heterogeneity is evaluated. We have highlighted the graphite strips in the figures to visualize them better. The permeability for the region with graphite strip was 2.083×10^{-8} m^2, which was calculated by assuming that the subsection behaves like an independent miniature Hele-Shaw cell with an aperture size of 0.05 mm by using **Eq. 1**. Additionally, to determine the effective permeability of the Hele-Shaw cell, we consider the permeability of both the regions with and without the graphite strips and calculate the weighted average based on the area. The updated porosity is calculated as the ratio of available volume inside the Hele-Shaw to the total volume and is found to be 0.948. The effective permeability for the medium with heterogeneities is calculated as 7.68×10^{-8} m^2, with a corresponding Rayleigh number of 40663, which is lower than the permeability and Ra number obtained for our homogeneous cases by 7.72% and 2.68%, respectively. Although the permeability calculated using this method may not strictly represent the actual permeability due to the associated boundary effects, the overall trend remains valid.

6.1. Effect of Heterogeneity (Case C1, C2, C3, and C4)

Fig. 13 displays the CO_2 dissolution behavior in the presence of heterogeneous barriers. The downward velocity of the fingers is slowed down along with decreased CO_2 dissolution, as evidenced by the smaller pH-depressed region compared to the homogenous case. Furthermore, as shown in **Fig. 13 (e-h),** upon passing the first set of heterogeneous layers, rather than traveling downwards vertically, the CO_2 finger moves in a curved manner towards the side of the heterogenous strips in the second layer. The curved finger travel alludes to a preferential CO_2 movement path, which can vary on the geometry of the heterogeneity. Heterogeneity also promotes flow channeling, resulting in a large region that CO2 does not encounter.

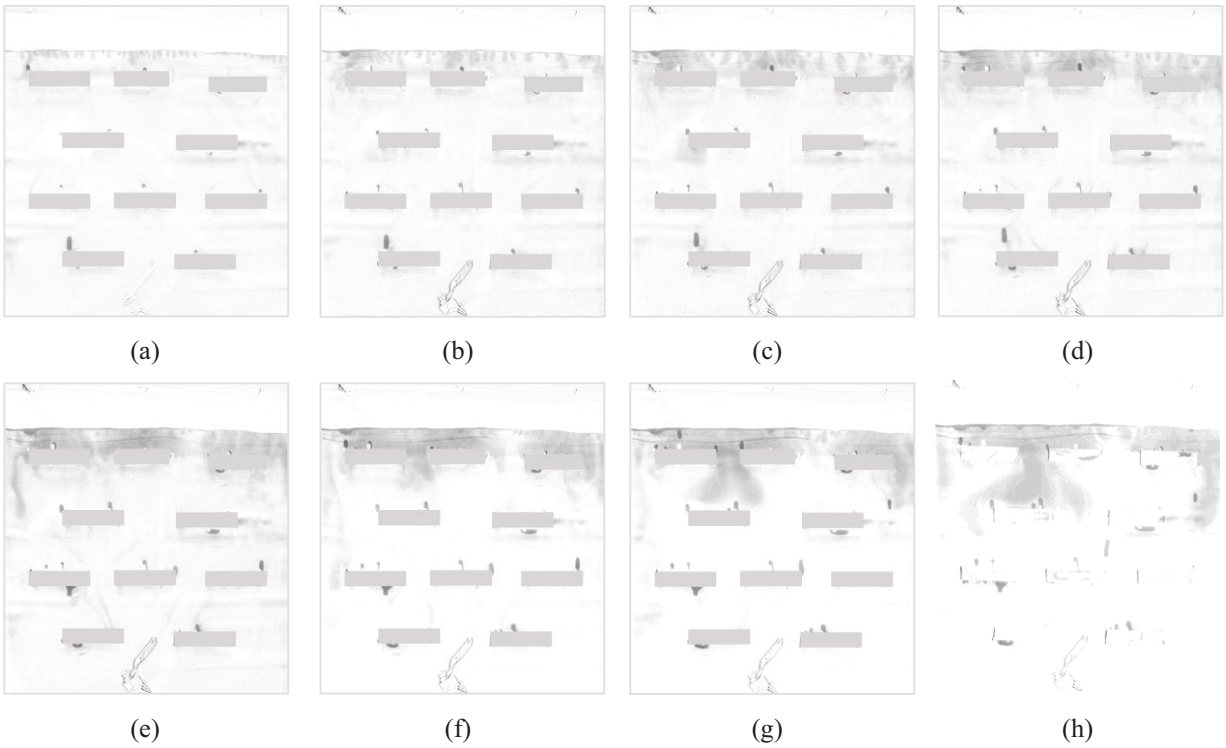

Figure 13. CO_2 introduced to the side of the cell at 0.59 L/min (CF, 1 mm aperture, vertically oriented flat glass with heterogeneous layers, **Case C1**) (a) 9 minutes (b) 15 minutes (c) 24 minutes (d) 36 minutes (e) 58 minutes (f) 85 minutes (g) 118 minutes (h) 154 minutes

Fig. 14, 15, and **16** represent the CO_2 dissolution behavior in the presence of 1M $CaCl_2$ solution, 1M $MgCl_2$ solution, and 1M NaCl solution, respectively. For NaCl and $CaCl_2$, as the convection is slower than CF, the lateral merging of CO_2 fingers is more dominant once it encounters the heterogeneous barrier. However, as shown in **Fig. 15**, for $MgCl_2$,

the vertical movement is more dominant compared to both NaCl and $CaCl_2$. This prevalent vertical finger travel for 1M $MgCl_2$ solutions can be attributed to faster CO_2 dissolution in the $MgCl_2$ solution than in NaCl and $CaCl_2$ solutions. The more rapid dissolution allows the fingers to quickly pass the heterogeneous barriers, leaving less time for lateral mixing.

Figure 14. CO_2 introduced to the side of the cell at 0.59 L/min (1 mole $CaCl_2$ dissolved CF- 1 mm aperture, vertically oriented flat glass with heterogeneous layers, **Case C2**) (a) 9 minutes (b) 15 minutes (c) 24 minutes (d) 36 minutes (e) 58 minutes (f) 85 minutes (g) 118 minutes (h) 154 minutes

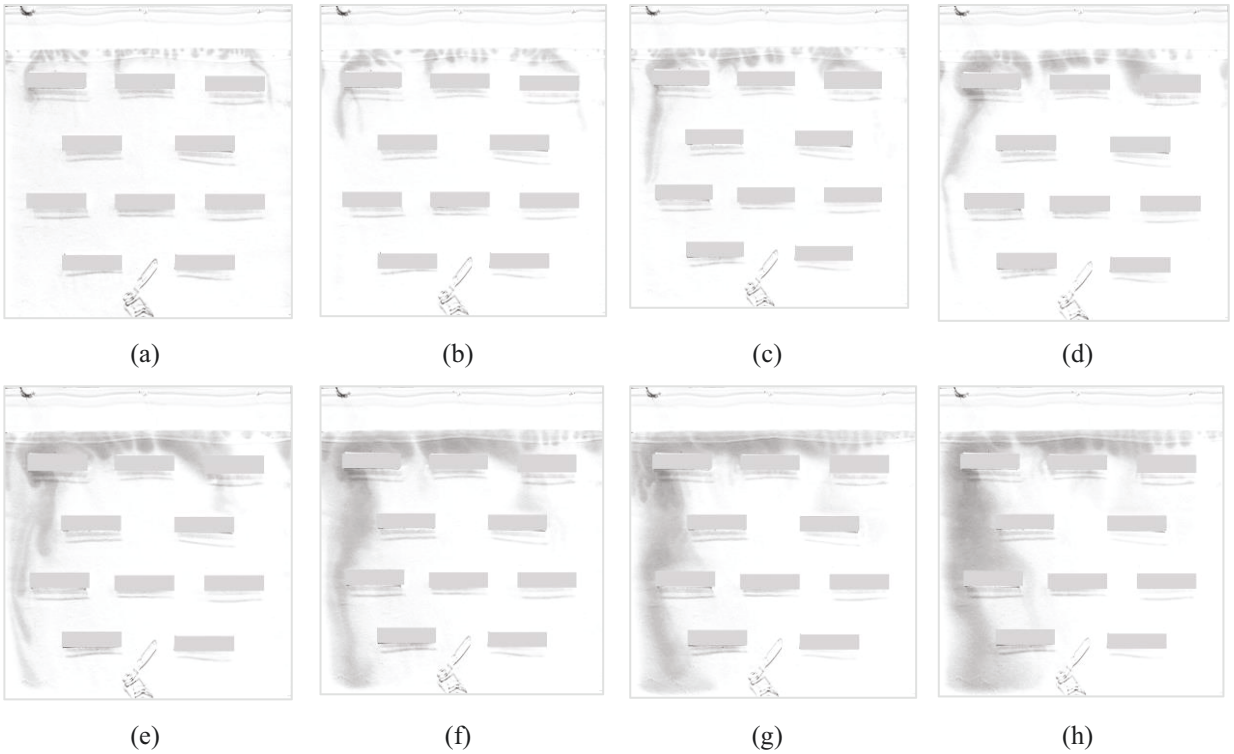

Figure 15. CO_2 introduced to the side of the cell at 0.59 L/min (1 mole $MgCl_2$ dissolved CF- 1 mm aperture, vertically oriented flat glass with heterogeneous layers, **Case C3)** (a) 9 minutes (b) 15 minutes (c) 24 minutes (d) 36 minutes (e) 58 minutes (f) 85 minutes (g) 118 minutes (h) 154 minutes

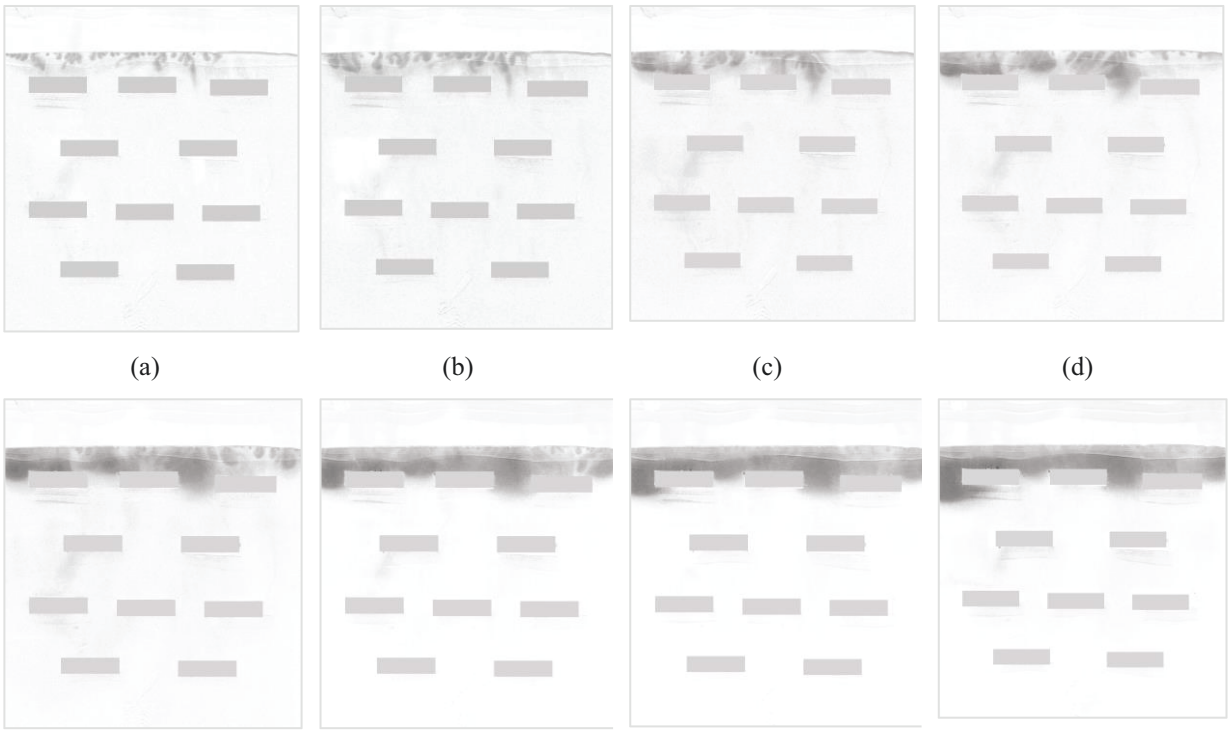

(e) (f) (g) (h)

Figure 16. CO_2 introduced to the side of the cell at 0.59 L/min (1 mole NaCl dissolved CF- 1 mm aperture, vertically oriented flat glass with heterogeneous layers, **Case C4)** (a) 9 minutes (b) 15 minutes (c) 24 minutes (d) 36 minutes (e) 58 minutes (f) 85 minutes (g) 118 minutes (h) 154 minutes

6.2. Effect of Fractures in Heterogeneous Layers (Case D1)

Information about natural fractures and their interaction with CO_2-acidified brine in the subsurface can play a crucial role in assessing the CO_2 storage parameters. Compared to the surrounding rock matrix, natural fractures in the geothermal reservoirs have a higher permeability region [73]. Fractures also have high conductivity, and the presence of an interconnected fracture system can provide potential CO_2 escape routes during storage by promoting the increased spatial spreading of CO_2 plume, thus allowing CO_2 migration pathway through the cap rocks to neighboring aquifers or surfaces [45,74].

Despite the recognized importance of heterogeneous layers, the impact of fractures present in these heterogeneous formations on the convective-flow pattern has not been visually studied extensively [40,41]. Therefore, we study the effect of fractures in heterogeneous regions by creating thin slits (4 mm spacing at 45° angle) between the graphite shims, as shown in **Fig. 17**. **Fig. 17** shows that the CO_2 spatial spreading is much faster due to the fractures compared to cases without fractures in heterogeneity (**Case C1-4**). This can be attributed to an increase in effective permeability in the system. The regions underneath the top fracture layer show the point of the CO_2 dissolution path, as new CO_2 fingers are visible underneath them in **Fig. 17 (b).** Alluding to the channeling effect, a preferential dissolution path is clearly visible around an hour into the experiment shown in **Fig. 17 (e**).

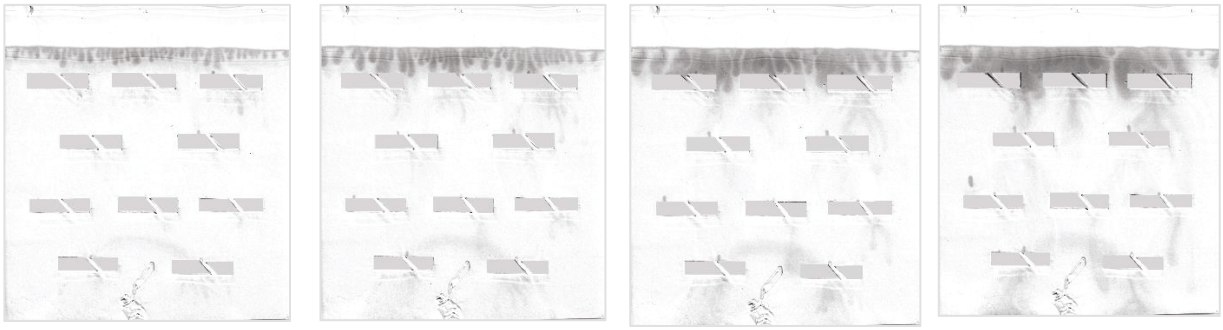

(a) (b) (c) (d)

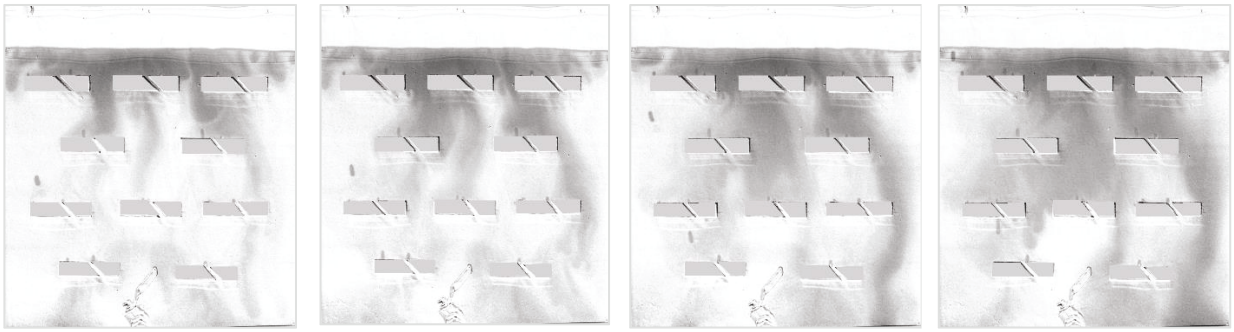

(e) (f) (g) (h)

Figure 17. CO_2 introduced to the side of the cell at 0.59 L/min (CF- 1 mm aperture, vertically oriented flat glass with fractured heterogeneous layers, **Case D1**) (a) 9 minutes (b) 15 minutes (c) 24 minutes (d) 36 minutes (e) 58 minutes (f) 85 minutes (g) 118 minutes (h) 154 minutes

7. Quantitative measurements

The number of fingers formed, average finger length (mm), average wavelength (mm), and standard deviation of finger length are the parameters that characterize the finger evolution dynamics. Finger length is calculated as the vertical distance from the interface to the tip of the finger. In contrast, the average wavelength is the interface length divided by the number of fingers. It should be noted that fingers with different tips at the end moving in different directions are considered separate fingers in this study.

Before presenting the results of our experimental investigations, we perform a repeatability test for the quantitative data (refer to **Fig. 4**). As shown in **Fig. 18**, for the three runs, we calculate the average of the finger parameters and consider the deviation with a 95% confidence interval. Although we observed a slight difference in the number of fingers formed initially, the deviation becomes negligible in the middle and later parts of the experiment. We also observed a deviation from the mean finger length value in the latter part of the experiment. This deviation in the early part of the experiment can be due to the uncertain nature of convective finger merging and flow patterns as the finger grows. The acceptable level of deviation observed in **Fig. 18** shows the repeatability of our experiments.

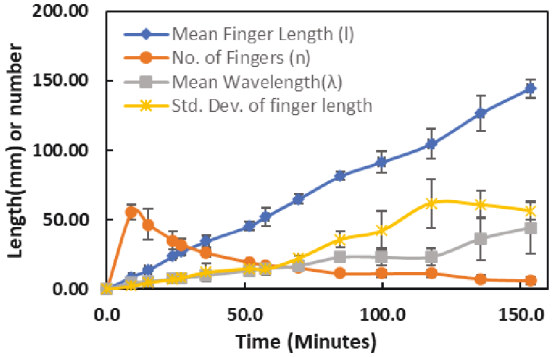

Figure 18. Quantitative data of the finger length parameters for the repeatability experiments.

7.1. Effect of injection point and presence of salt

The image analysis for **Case A1-A3** (**Fig. 19 a and b**) reveals average finger length having a similar trend, which denotes that the average finger length formation is independent of the injection point. Moreover, the number of fingers formed remains similar, regardless of the CO_2 injection point. However, the standard deviation of finger length is higher when CO_2 is injected into the left side of the cell. This is because the fingers underneath the CO_2 injection point quickly grew in size while the area on the right side observed less CO_2 dissolution, causing a higher imbalance in finger size.

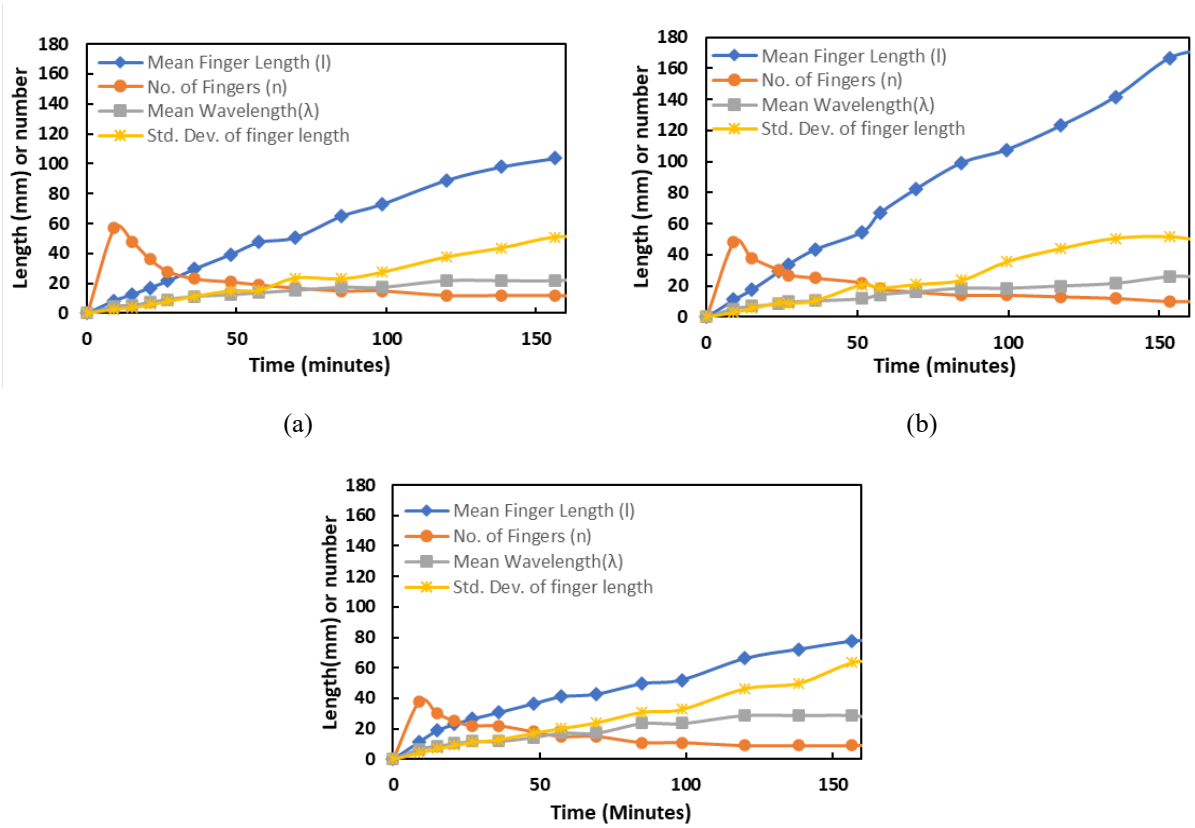

Figure 19. Number of fingers formed, wavelength, and finger length parameters for (a) Case A1 - CO_2 introduced to the side of the cell and (b) Case A2 - CO_2 introduced to the center of the cell (c) Case A3- 1 mole $CaCl_2$ dissolved in CF - CO_2 introduced to the center of the cell

The effect of salinity on finger evolution can be observed in **Fig. 19 (c)**. The effect of convection is attenuated due to the presence of $CaCl_2$, resulting in less finger interaction than in the control fluid. This is evident by the reduced number of fingers formed. Similar effects of salt were observed in other studies [34–36]. A higher standard deviation

of finger length is also observed due to the significant difference in finger size between the active zone (area under the CO_2 injection point) and the inactive zones (area at the side of the Hele-Shaw cells).

7.2. Effect of different salts with varying concentrations

To illustrate the effect of the presence of different salts with varying concentrations, the pH-depressed region for **Case B1-B4** is calculated and compared with the CO_2 dissolution in the CF. **Fig. 20** shows the results normalized with respect to the pH-depressed area for the CF. CO_2 is injected at the side of the Hele-Shaw cell for all the experiments, to control the effect of different injection points on the convective-dissolution pattern. It should be noted that a higher pH-depressed area refers to more CO_2 dissolution. As seen in **Fig. 20**, higher concentration leads to slower CO_2 dissolution for the same salt type, which is in perfect agreement with other studies [34,35,52]. The CO_2 dissolved area indicated by the pH-depressed region follows the order of $CaCl_2$ 2M solution < $MgCl_2$ 2M solution < $CaCl_2$ 1M solution < $MgCl_2$ 1M solution. At the beginning part of the experiment, all the salt types have almost similar dissolution areas. It can be due to the impact of minimal convection-driven flow at the beginning of the experiment. Therefore, it can be safe to assume that the effect of salinity is not significant throughout the induction phase and for a small period after the onset of convection.

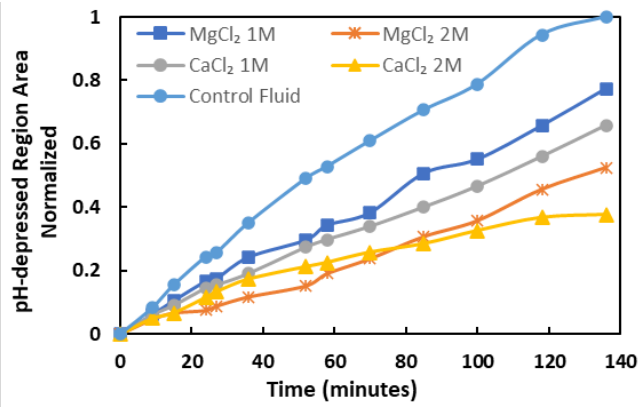

Figure 20. Area of the pH-depressed region (normalized) for different salts with varying concentration

The downward progression of fingers (also referred to as 'mixing length' by Thomas et al. [35]) is another factor worthy of investigation as it relates to the depth of investigation during CO_2 storage. To calculate the downward progression of the fingers, we consider the distance from the gas-water interface to the tip of the longest finger for any time, presented in **Fig. 21 (a)**. The vertical depth of investigation is quite similar for the CF, $CaCl_2$ 1M, and $MgCl_2$ 1M solutions. However, at higher concentrations ($CaCl_2$ 2M solution and $MgCl_2$ 2M solution), we observe a significant

582 decrease in the vertical progression of fingers. Using NaCl with varying concentrations, Thomas et al. observed a
583 similar effect [33]. Increasing salinity slows the convective flow, causing less CO_2 to dissolve, consequently reducing
584 the vertical depth of investigation. It should also be noted that dipping can reduce the vertical depth of investigation,
585 as it promotes lateral mixing over vertical travel.

586 Another interesting phenomenon can be observed while considering the earlier part of the experiments,
587 indicated by the red squared box in **Fig. 21 (a)**, also magnified as presented in **Fig. 21 (b)**. As shown in **Fig. 21 (b)**,
588 although the higher salt concentration in solution leads to a less vertical progression of fingers, the temporal finger
589 evolution is higher at the earlier stage, also clearly observable from the velocity of finger evolution shown in **Fig. 22**.
590 This indicates that the presence of salt enhances the diffusive flux which is the dominant mass-transfer method at an
591 earlier stage. However, as time progresses, convection flows become the predominant flow causing the finger
592 progression rate to slow. This experimental investigation also perfectly agrees with Kim and Kim's observation from
593 the numerical simulation [36].

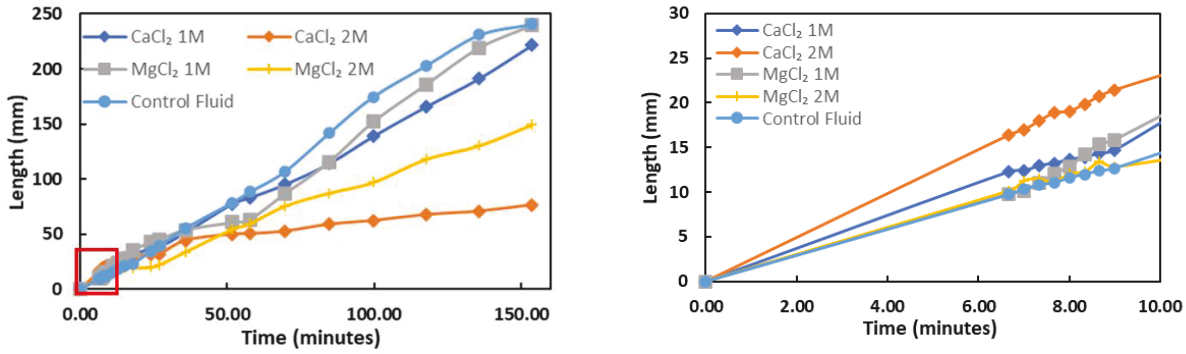

(a) (b)

594 **Figure 21.** (a) Temporal evolution of the vertical progression of fingers for different cases (b) Magnified view of the red squared region

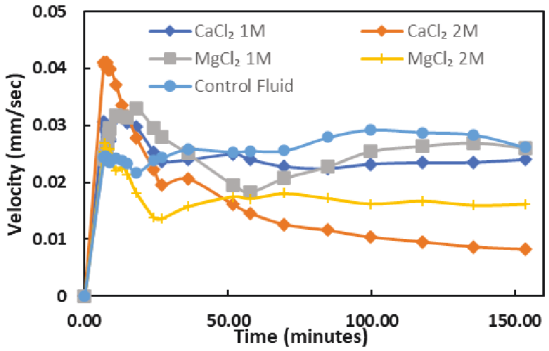

595

Figure 22. The velocity of vertical finger evolution for different cases

Fig. 23 presents the image analysis result for the salts with different concentrations. We observe a slow increase in the mean finger length at the beginning of the experiment, and the number of fingers decreases as the neighboring fingers merge. However, after around 36 minutes, the nascent fingers with short finger lengths start to appear at the gas-water interface, which reduces the mean finger length. Moreover, the mature fingers start to merge, resulting in fewer dominant fingers, further decreasing the mean finger length, which is the weighted average of all the fingers. However, it should be noted that despite our observation of a reduction in the mean finger length, there is still vertical progression of fingers throughout the experiment, as evident in **Fig. 21**. This trend continues throughout the latter part of the experiment, as the larger finger merges and forms the oval shape formation, there is a noticeable decrease in the mean finger length, also causing a sharp increase in the standard deviation. Moreover, as the contributing factor in determining mean finger length is the vertical finger travel, the lateral mixing of fingers due to the dipping angle also causes a reduction in the mean finger length.

The convective finger formation and dissolution rate depend significantly on the type and concentration of salt in the CF. **Fig 23 (b)** shows that the number of fingers formed is considerably slowed in case of a higher concentration of $CaCl_2$. There is a sharp increase in the number of fingers formed between 52 and 58 minutes since the fingers on the right side became apparent in that period. This shows that the CO_2 dissolution rate on the right side is significantly lower than on the left. Both the injection point and the presence of a dipping angle can cause this variance in dissolution rate.

Fig. 23 shows that the number of fingers formed for $MgCl_2$ is almost similar to that of $CaCl_2$. In the latter half of the experiment, we observed the fingers in $MgCl_2$ having a higher mean finger length, particularly due to the faster vertical travel of the finger on the left side of the cell. Moreover, since the finger formation in the right side of the cell is significantly slow in all the cases, we observe a higher standard deviation in the later part of the experiment for the $MgCl_2$ experiments. Furthermore, the lower standard deviation of fingers in both the 2M solution cases can be attributed to the higher salinity and dipping angle preventing vertical travel and promoting lateral mixing of the fingers.

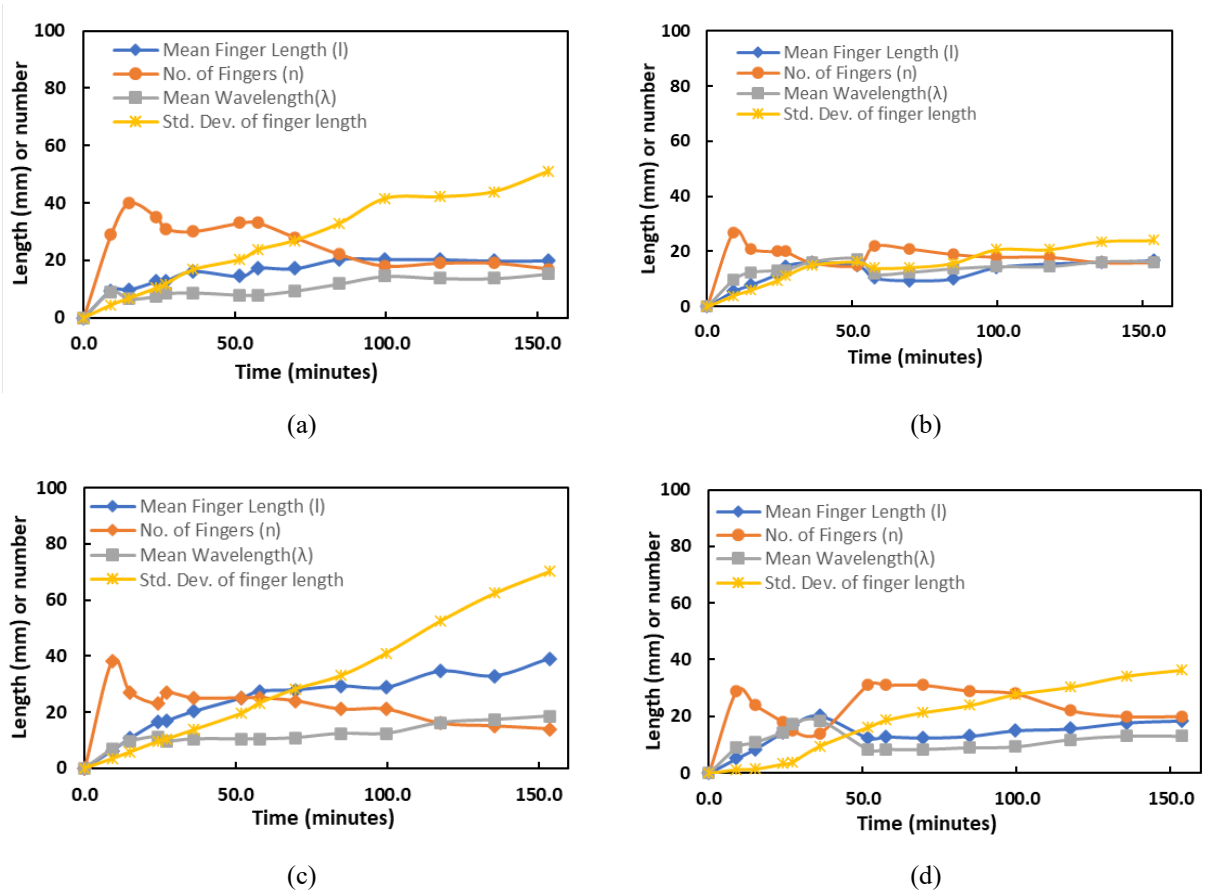

620 **Figure 23.** Number of fingers formed, wavelength and finger length parameters for (a) 1 mole $CaCl_2$ dissolved in Control Fluid – CO_2
621 introduced to the side of the cell and (b) 2 mole $CaCl_2$ dissolved in Control Fluid – CO_2 introduced to the side of the cell (c) 1 mole $MgCl_2$
622 dissolved in Control Fluid – CO_2 introduced to the side of the cell (d) 2 mole $MgCl_2$ dissolved in Control Fluid – CO_2 introduced to the side of
623 the cell

624 ## 8. Discussion

625 The structural morphology (formation dipping angle, pore-networks), geological properties (rock porosity,
626 permeability, presence of fractures or barriers, etc.), and the accurate geochemical composition of the storage site play
627 a significant role in transporting and storing CO_2 in the brine in dissolved form. Therefore, a fundamental
628 understanding of these parameters and their role in convective CO_2 transport is essential to optimize the existing CO_2
629 storage operations and select appropriate new CO_2 storage sites. In addition, understanding the horizontal migration
630 of supercritical CO_2 plumes due to structural dipping and point of injection is essential to reduce the chance of CO_2
631 leakage from fractured caprocks. The empirical observations of the parameters made in our study are summarized and

presented in **Table 3**. This study critically evaluates these parameters to provide some important insights, which are discussed below:

8.1. Effect of salt concentration and dipping angle on convective dissolution

Our study showed that the presence of salts could significantly slow the convective flow, and the convective flow rate can depend on the salt type and its concentration. The CO_2 dissolution pattern was also noticeably different in the presence of salt, moving in a piston-like-displacement manner. Although the convective flow is slowed down, we observed enhanced diffusive flux, the dominant mass-transfer method at the earlier stage of CO_2 storage. Comparing the convective CO_2 flow pattern without and with salts with different concentrations, we can conclude that lower salinity storage sites are more favorable for safe CO_2 storage, despite benefits like faster dissolution and earlier onset time of convection.

Table 3. Empirical observations on the parameters observed

Parameters Observed	**Empirical Observations**
CO_2 Injection Point	• Injection point near boundary has different convective flow pattern than injection at the middle
Salinity	• Enhances the diffusive flux • Slows down the convective flow • Reduces CO_2 dissolution rate with increasing salinity
Dipping	• Promotes lateral mixing compare to vertical finger travel • Reduces CO_2 storage with increasing dipping angle (however, the effect is not as significant as salinity)
Fractures	• Promotes high spatial CO_2 plume spreading • Highly fractured regions have a high risk of CO_2 leakage during storage
Heterogeneity	• Different convection flow patterns are possible based on heterogeneous patterns

	• Uneven CO_2 sweep with large unaffected regions

Even though most of the experimental studies and simulations generalize geological storage sites to be horizontal, the majority of the sites have gradients as an effect of diagenesis and other geological phenomena. Although the effect of dip angle is less significant than that of salinity, the presence of the formation dip can significantly impact the space migration of CO_2 mixed fluid flow, as observed in our study. Due to the dominance of lateral mixing of CO_2 fingers over vertical travel, where dipping is involved, the depth of investigation is reduced for storage sites with a formation angle. A larger formation dip angle is not conducive to CO_2 geological storage as it promotes spatial CO_2 migration, risking long-term CO_2 storage. Further experimental studies on the effect of dipping angles on the depth of investigation can be done at a field-scale level for better theoretical benchmarking.

8.2. Effect of flow barriers (boundary, heterogeneities, and fractures) on convective dissolution

In our study, the injection point near the boundary had a considerably different convective flow pattern than the injection in the middle. From this visual investigation, we can infer that the vertical faults present at the storage site can cause a change in the convective flow pattern. Additionally, our characterization of convective flow for heterogeneities with fractures reveals how the CO_2 plume can migrate/spread through the fractures. Since the fractured regions can be highly conductive and increase CO_2 spatial spreading, fractures are not conducive to CO_2 storage. In addition, the formation of preferential channels for CO_2-acidified fluid flow is also observed. However, it should be noted that the channel growth and preferential fluid flow are more complex in storage sites and thus needs more attention.

Furthermore, the convective-flow pattern and the effective permeability of the storage site can vary significantly based on the fracture patterns. Therefore, the fraction patterns used to derive correlations will only apply to reservoirs with a similar pattern, showing the importance of considering all possible fracture network characteristics to critically estimate and model the complex fracture geometry for a particular storage site.

8.3. Effect of Higher Pressure and Temperature

CO_2 storage sites have higher pressure and temperature than atmospheric conditions, leading to several studies focusing on the effects of high pressure and high temperature (HPHT) on CO_2 dissolution. Outeda et al. [16] investigated the impact of varied pressure (1.5-5 bar) on CO_2 dissolution at a constant temperature of 25 ºC. Increasing pressure resulted in high CO_2 mass influx to the aqueous phase, increasing mixing length. Furthermore, instabilities are noticed earlier at higher pressure. At the lowest pressure of 1.5 bar, the instabilities were observable at around 60 s, whereas, for 5 bar, the instabilities could be seen as early as 10 s. However, factors like the wavelength of fingers or shape were independent of pressure change. Another CO_2 dissolution study at HPHT condition (140-240 bar and 20-150 ºC) by Tang et al. [4] showed that increasing pressure resulted in a higher Rayleigh number. Moreover, the study concluded that pressure has a larger influence on CO2 solubility than the diffusion coefficient at reservoir HPHT condition.

Despite considerable CO_2 dissolution visualization studies being performed, most do not consider a porous medium. Therefore Amarasinghe et al. [53] investigated CO_2 dissolution in a porous media using 400-600 µm glass beads at 105 bar and 50 ºC. The results were compared to Vosper et al. [75], who used similar glass bead sizes but different atmospheric conditions (1 bar and room temperature). A comparison of the results revealed that the CO_2 transport rate is considerably higher at higher pressure and temperature (HPHT) conditions (reaching a depth of 40 mm in 20 minutes) compared to atmospheric conditions (reaching 40 mm in 100 minutes). This higher transport rate is also attributed to CO_2 being supercritical at the HPHT condition. Amarasinghe et al. [13] also investigated CO_2 transport in heterogeneous porous media by packing the Hele-Shaw cell with glass beads of different permeability at 100 bar and 50 ºC.

The effect of brine composition on CO_2 dissolution at 34.5-36.9 bar and 50 °C was investigated in the works of Mahmoodpour et al. [62]. They observed a late onset time of convection and lower finger growth rate in solutions containing NaCl and $CaCl_2$ at HPHT conditions, similar to our experimental observations at atmospheric conditions. Furthermore, a study by Jiang et al. [14] at 38 ºC and 90-110 bar reached similar findings, showing that CO_2 solubility is higher at high pressure, leading to faster CO_2 solution accumulation at the top interface. Furthermore, under supercritical pressure, the density difference of the CO_2 solution is considerably higher, thus promoting finger formation and development. In contrast, salinity seemed to inhibit finger formation and migration.

The findings from the CO_2 dissolution studies under HPHT conditions show that higher pressure and temperature are favorable for faster CO_2 transport. However, since there is no significant change in finger morphology due to variation in pressure and temperature, it is safe to assume that the fundamental aspects of reactive-convective transport in atmospheric conditions found in this study will also hold in high-pressure and temperature conditions. Future studies will consider a more complicated interpretation involving quantitative analyses with the effect of different salt types and concentrations at high pressure and supercritical conditions.

9. Conclusion

This study provided a visual investigation into the effects of different parameters that dictates the CO_2 geologic storage: injection point and pressure, presence of salts with varying concentration, and presence of heterogeneities and dipping angle using the Hele-Shaw cell. Moreover, quantitative results were provided, which can be used for theoretical modeling. Our results show favorable conditions for CO_2 geological storage, including none or low reservoir dipping. Furthermore, the absence of salinity is preferable; however, since all geological storage aquifer fluids will have some dissolved salts, selections should be made based on reservoirs with the lowest salinity. We observed the qualitative onset time of convection at around 135 s with a corresponding finger wavelength of 3.56-5.3 mm. In the presence of salt, the convection initiated at about 105 s with a corresponding finger wavelength of 6.33 mm. This difference shows that the initial diffusion is higher in brine with high salt concentrations but does not translate to enhanced convection and dissolution. The CO_2 dissolved area for different salts, indicated by the pH-depressed region, are considerably smaller than when no salt is present, and it follows the order of $CaCl_2$ 2M solution < $MgCl_2$ 2M solution < $CaCl_2$ 1M solution < $MgCl_2$ 1M solution. A factor not considered in this study but worthy of further investigation is the synergistic effect of multiple salts in saline aquifers which can be studied by creating solutions with a chemical composition similar to the brine by mixing several salts. By identifying the critical factors controlling the convective mixing, this study also provides new insights into the possible line of future work on the transport mechanisms during dissolution-driven CO_2 convective flow.

Acknowledgements:

We would like to thank Mr. Edward Farina from the UT Tyler Machine Shop for his significant help with the material selection, fabrication, and troubleshooting of the apparatus used in this study. We thank the anonymous reviewers for their edits and suggestions, which improved our manuscript. This material is based upon work partly supported by the

National Science Foundation Award under CBET-2245484. Any opinions, findings, and conclusions or recommendations expressed in this material are those of the author(s) and do not necessarily reflect the views of the National Science Foundation.

Table of Abbreviations

2D	Two Dimensional
3D	Three Dimensional
BCG	Bromocresol Green
$CaCl_2$	Calcium Chloride
CCS	Carbon Capture and Storage
CF	Control Fluid
CO_2	Carbon Dioxide
HPHT	High Pressure and High Temperature
$KMnO_4$	Potassium Permanganate
LIF	Laser-Induced Fluorescence
NaCl	Sodium Chloride
PIV	Particle Image Velocimetry
PVT	Pressure-Volume-Temperature
Ra	Rayleigh number
RC	Rayleigh convection

RGB	Red-Green-Blue
sCO_2	Supercritical CO_2
UV	Ultraviolet

726

References

[1] M.F. Shahriar, A. Khanal, The current techno-economic, environmental, policy status and perspectives of sustainable aviation fuel (SAF), Fuel. 325 (2022) 124905. https://doi.org/10.1016/j.fuel.2022.124905.

[2] Z. Zhang, Q. Fu, H. Zhang, X. Yuan, K.T. Yu, Experimental and Numerical Investigation on Interfacial Mass Transfer Mechanism for Rayleigh Convection in Hele-Shaw Cell, Ind. Eng. Chem. Res. 59 (2020) 10195–10209. https://doi.org/10.1021/acs.iecr.0c01345.

[3] A. Khanal, M.F. Shahriar, Physics-Based Proxy Modeling of CO2 Sequestration in Deep Saline Aquifers, Energies. 15 (2022) 4350. https://doi.org/10.3390/en15124350.

[4] Y. Tang, Z. Li, R. Wang, M. Cui, X. Wang, Z. Lun, Y. Lu, Experimental Study on the Density-Driven Carbon Dioxide Convective Diffusion in Formation Water at Reservoir Conditions, ACS Omega. 4 (2019) 11082–11092. https://doi.org/10.1021/acsomega.9b00627.

[5] R. Khosrokhavar, G. Elsinga, R. Farajzadeh, H. Bruining, Visualization and investigation of natural convection flow of CO2 in aqueous and oleic systems, J. Pet. Sci. Eng. 122 (2014) 230–239. https://doi.org/10.1016/j.petrol.2014.07.016.

[6] R. Khosrokhavar, A. Eftekhari, R. Farajzdadeh, K.H. Wolf, H. Bruining, Effect of Salinity and Pressure on the Rate of Mass Transfer in Aquifer Storage of CO2, IOR 2015 - 18th Eur. Symp. Improv. Oil Recover. (2015). https://doi.org/10.3997/2214-4609.201412114.

[7] H. Emami-Meybodi, Stability analysis of dissolution-driven convection in porous media, Phys. Fluids. 29 (2017). https://doi.org/10.1063/1.4974275.

[8] C.A. Dorao, Dispersion phenomena in gas liquid systems, J. Nat. Gas Sci. Eng. 5 (2012) 25–30. https://doi.org/10.1016/j.jngse.2011.08.004.

[9] M.R. Soltanian, M.A. Amooie, Z. Dai, D. Cole, J. Moortgat, Critical Dynamics of Gravito-Convective Mixing in Geological Carbon Sequestration, Sci. Rep. 6 (2016) 35921. https://doi.org/10.1038/srep35921.

[10] A. Taheri, O. Torsæter, E. Lindeberg, N.J. Hadia, D. Wessel-Berg, Qualitative and quantitative experimental study of convective mixing process during storage of CO2 in heterogeneous saline aquifers, Int. J. Greenh.

752 Gas Control. 71 (2018) 212–226. https://doi.org/10.1016/j.ijggc.2018.02.003.

753 [11] A. Taheri, O. Torsæter, D. Wessel-Berg, M. Soroush, Experimental and Simulation Studies of Density-
754 Driven-Convection Mixing in a Hele-Shaw Geometry with Application for CO2 Sequestration in Brine
755 Aquifers, in: All Days, SPE, 2012. https://doi.org/10.2118/154908-MS.

756 [12] W. Amarasinghe, I. Fjelde, Y. Guo, CO2 dissolution and convection in oil at realistic reservoir conditions: A
757 visualization study, J. Nat. Gas Sci. Eng. 95 (2021). https://doi.org/10.1016/j.jngse.2021.104113.

758 [13] W.S. Amarasinghe, I. Fjelde, A.M.N. Flaata, Visual investigation of CO2 dissolution and convection in
759 heterogeneous porous media at reservoir temperature and pressure conditions, Greenh. Gases Sci. Technol.
760 11 (2021) 342–359. https://doi.org/10.1002/ghg.2055.

761 [14] L. Jiang, Y. Wang, G. Lu, J. Yang, Y. Song, Experimental Study on the Density-Driven Convective Mixing
762 of CO2 and Brine at Reservoir Temperature and Pressure Conditions, Energy and Fuels. (2022).
763 https://doi.org/10.1021/acs.energyfuels.2c00054.

764 [15] B. An, D. Solorzano, Q. Yuan, Viscous Fingering Dynamics and Flow Regimes of Miscible Displacements
765 in a Sealed Hele-Shaw Cell, Energies. 15 (2022) 5798. https://doi.org/10.3390/en15165798.

766 [16] R. Outeda, C. El Hasi, A. D'Onofrio, A. Zalts, Experimental study of linear and nonlinear regimes of density-
767 driven instabilities induced by CO(2) dissolution in water, Chaos. 24 (2014) 013135.
768 https://doi.org/10.1063/1.4868040.

769 [17] A. Singh, Y. Singh, K.M. Pandey, Viscous fingering instabilities in radial Hele-Shaw cell: A review, Mater.
770 Today Proc. 26 (2019) 760–762. https://doi.org/10.1016/j.matpr.2020.01.022.

771 [18] M. De Paoli, M. Alipour, A. Soldati, How non-Darcy effects influence scaling laws in Hele-Shaw convection
772 experiments, J. Fluid Mech. (2020). https://doi.org/10.1017/jfm.2020.229.

773 [19] M.C. Kim, Linear and nonlinear analyses on the onset of gravitational instabilities in a fluid saturated within
774 a vertical Hele-Shaw cell, Chem. Eng. Sci. 126 (2015) 349–360. https://doi.org/10.1016/j.ces.2014.12.032.

775 [20] T.J. Kneafsey, K. Pruess, Laboratory experiments and numerical simulation studies of convectively enhanced
776 carbon dioxide dissolution, Energy Procedia. 4 (2011) 5114–5121.

https://doi.org/10.1016/j.egypro.2011.02.487.

[21] S. Backhaus, K. Turitsyn, R.E. Ecke, Convective instability and mass transport of diffusion layers in a Hele-Shaw geometry, Phys. Rev. Lett. 106 (2011) 1–4. https://doi.org/10.1103/PhysRevLett.106.104501.

[22] A.C. Slim, M.M. Bandi, J.C. Miller, L. Mahadevan, Dissolution-driven convection in a Hele-Shaw cell, Phys. Fluids. 25 (2013). https://doi.org/10.1063/1.4790511.

[23] S. Mojtaba, R. Behzad, N.M. Rasoul, R. Mohammad, Experimental study of density-driven convection effects on CO2 dissolution rate in formation water for geological storage, J. Nat. Gas Sci. Eng. 21 (2014) 600–607. https://doi.org/10.1016/j.jngse.2014.09.020.

[24] T.F. Faisal, S. Chevalier, Y. Bernabe, R. Juanes, M. Sassi, Quantitative and qualitative study of density driven CO2 mass transfer in a vertical Hele-Shaw cell, Int. J. Heat Mass Transf. 81 (2015) 901–914. https://doi.org/10.1016/j.ijheatmasstransfer.2014.11.017.

[25] H. Wang, F. Torabi, F. Zeng, H. Xiao, Experimental and numerical study of non-equilibrium dissolution and exsolution behavior of CO2 in a heavy oil system utilizing Hele-Shaw-like visual cell, Fuel. 270 (2020). https://doi.org/10.1016/j.fuel.2020.117501.

[26] M.C. Kim, C. Wylock, Linear and nonlinear analyses of the effect of chemical reaction on the onset of buoyancy-driven instability in a CO 2 absorption process in a porous medium or Hele-Shaw cell, Can. J. Chem. Eng. 95 (2017) 589–604. https://doi.org/10.1002/cjce.22694.

[27] S. Mahmoodpour, B. Rostami, M.R. Soltanian, M.A. Amooie, Convective Dissolution of Carbon Dioxide in Deep Saline Aquifers: Insights from Engineering a High-Pressure Porous Visual Cell, Phys. Rev. Appl. 12 (2019). https://doi.org/10.1103/PhysRevApplied.12.034016.

[28] G.S.H. Pau, J.B. Bell, K. Pruess, A.S. Almgren, M.J. Lijewski, K. Zhang, High-resolution simulation and characterization of density-driven flow in CO2 storage in saline aquifers, Adv. Water Resour. 33 (2010) 443–455. https://doi.org/10.1016/j.advwatres.2010.01.009.

[29] A.C. Slim, Solutal-convection regimes in a two-dimensional porous medium, J. Fluid Mech. 741 (2014) 461–491. https://doi.org/10.1017/jfm.2013.673.

802 [30] C. Wylock, A. Rednikov, B. Haut, P. Colinet, Nonmonotonic Rayleigh-Taylor Instabilities Driven by Gas–
803 Liquid CO 2 Chemisorption, J. Phys. Chem. B. 118 (2014) 11323–11329. https://doi.org/10.1021/jp5070038.

804 [31] X. Cao, M. Zhang, A.S. Mujumdar, Q. Zhong, Z. Wang, Effects of ultrasonic pretreatments on quality, energy
805 consumption and sterilization of barley grass in freeze drying, 2018.
806 https://doi.org/10.1016/j.ultsonch.2017.06.014.

807 [32] Z. Zhang, H. Zhang, X. Yuan, K.T. Yu, Effective UV-Induced Fluorescence Method for Investigating
808 Interphase Mass Transfer of Single Bubble Rising in the Hele-Shaw Cell, Ind. Eng. Chem. Res. 59 (2020)
809 6729–6740. https://doi.org/10.1021/acs.iecr.9b07106.

810 [33] C. Thomas, V. Loodts, L. Rongy, A. De Wit, Convective dissolution of CO2 in reactive alkaline solutions:
811 Active role of spectator ions, Int. J. Greenh. Gas Control. 53 (2016) 230–242.
812 https://doi.org/10.1016/j.ijggc.2016.07.034.

813 [34] V. Loodts, L. Rongy, A. De Wit, Impact of pressure, salt concentration, and temperature on the convective
814 dissolution of carbon dioxide in aqueous solutions, Chaos. 24 (2014). https://doi.org/10.1063/1.4896974.

815 [35] C. Thomas, S. Dehaeck, A. De Wit, Convective dissolution of CO2 in water and salt solutions, Int. J. Greenh.
816 Gas Control. 72 (2018) 105–116. https://doi.org/10.1016/j.ijggc.2018.01.019.

817 [36] M. Chan Kim, Y. Hwan Kim, The effect of chemical reaction on the onset of gravitational instabilities in a
818 fluid saturated within a vertical Hele-Shaw cell: Theoretical and numerical studies, Chem. Eng. Sci. 134
819 (2015) 632–647. https://doi.org/10.1016/j.ces.2015.05.066.

820 [37] J. Jing, Y.L. Yang, Z.H. Tang, Effects of formation dip angle and salinity on the safety of CO2 geological
821 storage - A case study of Shiqianfeng strata with low porosity and low permeability in the Ordos Basin, China,
822 J. Clean. Prod. 226 (2019) 874–891. https://doi.org/10.1016/j.jclepro.2019.04.038.

823 [38] F. Wang, J. Jing, T. Xu, Y. Yang, G. Jin, Impacts of stratum dip angle on CO2 geological storage amount and
824 security, Greenh. Gases Sci. Technol. 6 (2016) 682–694. https://doi.org/10.1002/ghg.1594.

825 [39] A. Kumar, M. Noh, G.A. Pope, K. Sepehrnoori, S. Bryant, L.W. Lake, Reservoir simulation of CO2 storage
826 in deep saline aquifers, SPE - DOE Improv. Oil Recover. Symp. Proc. (2004). https://doi.org/10.2118/89343-

ms.

[40] A. Khanal, R. Weijermars, Comparison of Flow Solutions for Naturally Fractured Reservoirs Using Complex Analysis Methods (CAM) and Embedded Discrete Fracture Models (EDFM): Fundamental Design Differences and Improved Scaling Method, Geofluids. 2020 (2020). https://doi.org/10.1155/2020/8838540.

[41] A. Khanal, R. Weijermars, Distinguishing Fracture Conductivity and Fracture Flux: A Systematic Investigation of Individual Fracture Contribution to Well Productivity, in: Proc. 8th Unconv. Resour. Technol. Conf., American Association of Petroleum Geologists, Tulsa, OK, USA, 2020. https://doi.org/10.15530/urtec-2020-2176.

[42] R. Weijermars, A. Khanal, Flow in fractured porous media modeled in closed-form: Augmentation of prior solution and side-stepping inconvenient branch cut locations, Fluids. 5 (2020). https://doi.org/10.3390/fluids5020051.

[43] R. Weijermars, A. Khanal, High-resolution streamline models of flow in fractured porous media using discrete fractures: Implications for upscaling of permeability anisotropy, Earth-Science Rev. 194 (2019) 399–448. https://doi.org/10.1016/j.earscirev.2019.03.011.

[44] C.E. Bond, R. Wightman, P.S. Ringrose, The influence of fracture anisotropy on CO2 flow, Geophys. Res. Lett. 40 (2013) 1284–1289. https://doi.org/10.1002/grl.50313.

[45] M. Iding, P. Ringrose, Evaluating the impact of fractures on the performance of the In Salah CO2 storage site, Int. J. Greenh. Gas Control. 4 (2010) 242–248. https://doi.org/10.1016/j.ijggc.2009.10.016.

[46] A. V. Gorin, On Analogy Between Convective Heat and Mass Transfer Processes in a Porous Medium and a Hele-Shaw Cell, in: 2012: pp. 139–159. https://doi.org/10.1007/978-3-642-21966-5_6.

[47] F. Graf, E. Meiburg, C. Härtel, Density-driven instabilities of miscible fluids in a Hele-Shaw cell: Linear stability analysis of the three-dimensional Stokes equations, J. Fluid Mech. 451 (2002) 261–282. https://doi.org/10.1017/s0022112001006516.

[48] L. Paterson, Fingering with miscible fluids in a Hele Shaw cell, Phys. Fluids. 28 (1985) 26–30. https://doi.org/10.1063/1.865195.

852 [49] R.L. Detwiler, S.E. Pringle, R.J. Glass, Measurement of fracture aperture fields using transmitted light: An
853 evaluation of measurement errors and their influence on simulations of flow and transport through a single
854 fracture, Water Resour. Res. 35 (1999) 2605–2617. https://doi.org/10.1029/1999WR900164.

855 [50] A. Khanal, M.F. Shahriar, Optimization of CO2 Huff-n-Puff in Unconventional Reservoirs with a Focus on
856 Pore Confinement Effects, Fluid Types, and Completion Parameters, Energies. 16 (2023) 2311.
857 https://doi.org/10.3390/en16052311.

858 [51] G. Lu, Y. Liu, L. Jiang, T. Ying, Y. Song, B. Wu, Study of Density Driven Convection in a Hele-Shaw Cell
859 with Application to the Carbon Sequestration in Aquifers, Energy Procedia. 114 (2017) 4303–4312.
860 https://doi.org/10.1016/j.egypro.2017.03.1576.

861 [52] T.J. Kneafsey, K. Pruess, Laboratory flow experiments for visualizing carbon dioxide-induced, density-driven
862 brine convection, Transp. Porous Media. 82 (2010) 123–139. https://doi.org/10.1007/s11242-009-9482-2.

863 [53] W. Amarasinghe, I. Fjelde, J.Å. Rydland, Y. Guo, Effects of permeability on CO2 dissolution and convection
864 at reservoir temperature and pressure conditions: A visualization study, Int. J. Greenh. Gas Control. 99 (2020).
865 https://doi.org/10.1016/j.ijggc.2020.103082.

866 [54] C. Thomas, L. Lemaigre, A. Zalts, A. D'Onofrio, A. De Wit, Experimental study of CO2 convective
867 dissolution: The effect of color indicators, Int. J. Greenh. Gas Control. 42 (2015) 525–533.
868 https://doi.org/10.1016/j.ijggc.2015.09.002.

869 [55] A. Taheri, E. Lindeberg, O. Torsæter, D. Wessel-Berg, Qualitative and quantitative experimental study of
870 convective mixing process during storage of CO2 in homogeneous saline aquifers, Int. J. Greenh. Gas Control.
871 66 (2017) 159–176. https://doi.org/10.1016/j.ijggc.2017.08.023.

872 [56] F. Liu, P. Lu, C. Zhu, Y. Xiao, Coupled reactive flow and transport modeling of CO2 sequestration in the Mt.
873 Simon sandstone formation, Midwest U.S.A., Int. J. Greenh. Gas Control. 5 (2011) 294–307.
874 https://doi.org/10.1016/j.ijggc.2010.08.008.

875 [57] Z. Li, M. Dong, S. Li, L. Dai, Densities and Solubilities for Binary Systems of Carbon Dioxide + Water and
876 Carbon Dioxide + Brine at 59 °C and Pressures to 29 MPa, J. Chem. Eng. Data. 49 (2004) 1026–1031.

https://doi.org/10.1021/je049945c.

[58] R.J. Rosenbauer, T. Koksalan, J.L. Palandri, Experimental investigation of CO2-brine-rock interactions at elevated temperature and pressure: Implications for CO2 sequestration in deep-saline aquifers, Fuel Process. Technol. 86 (2005) 1581–1597. https://doi.org/10.1016/j.fuproc.2005.01.011.

[59] B. Zerai, B.Z. Saylor, G. Matisoff, Computer simulation of CO2 trapped through mineral precipitation in the Rose Run Sandstone, Ohio, Appl. Geochemistry. 21 (2006) 223–240. https://doi.org/10.1016/j.apgeochem.2005.11.002.

[60] P. Ranganathan, P. Van Hemert, E.S.J. Rudolph, P.Z.J. Zitha, Numerical modeling of CO2 mineralisation during storage in deep saline aquifers, Energy Procedia. 4 (2011) 4538–4545. https://doi.org/10.1016/j.egypro.2011.02.411.

[61] G.P.D. De Silva, P.G. Ranjith, M.S.A. Perera, Geochemical aspects of CO2 sequestration in deep saline aquifers: A review, Fuel. 155 (2015) 128–143. https://doi.org/10.1016/j.fuel.2015.03.045.

[62] S. Mahmoodpour, B. Rostami, M.R. Soltanian, M.A. Amooie, Effect of brine composition on the onset of convection during CO 2 dissolution in brine, Comput. Geosci. 124 (2019) 1–13. https://doi.org/10.1016/j.cageo.2018.12.002.

[63] T. Xu, Y.-C.C. Jin, Simulation the convective mixing of CO2 in geological formations with a meshless model, Chem. Eng. Sci. 192 (2018) 187–198. https://doi.org/10.1016/j.ces.2018.07.016.

[64] A. Taheri, O. Torsæter, E. Lindeberg, N.J. Hadia, D. Wessel-Berg, Effect of Convective Mixing Process on Storage of CO2 in Saline Aquifers with Layered Permeability, Adv. Chem. Res. 3 (2021). https://doi.org/10.21926/acr.2101012.

[65] V. Loodts, C. Thomas, L. Rongy, A. De Wit, Control of Convective Dissolution by Chemical Reactions: General Classification and Application to <math display="inline"> <mrow> <msub> <mrow> <mi>CO</mi> </mrow> <mrow> <mn>2</mn> </mrow> </msub> </mrow> </math> Dissolution in Reactive Aqueous Solutions, Phys. Rev. Lett. 113 (2014) 114501. https://doi.org/10.1103/PhysRevLett.113.114501.

[66] L. Jiang, S. Wang, D. Liu, W. Zhang, G. Lu, Y. Liu, J. Zhao, Change in convection mixing properties with

902 salinity and temperature: CO2 storage application, Polymers (Basel). 12 (2020).
903 https://doi.org/10.3390/POLYM12092084.

904 [67] E. Lindeberg, D. Wessel-Berg, Upscaling studies of diffusion induced convection in homogeneous and
905 heterogeneous aquifers, Energy Procedia. 4 (2011) 3927–3934. https://doi.org/10.1016/j.egypro.2011.02.331.

906 [68] K. Pruess, K. Zhang, Numerical Modeling Studies of The Dissolution-Diffusion-Convection Process During
907 CO2 Storage in Saline Aquifers, Lawrence Berkeley Natl. Lab. (2008) 1–33.
908 papers2://publication/uuid/7D178882-C5E3-4A78-8B79-633C227DDED7.

909 [69] H. Qiblawey, M. Arshad, A. Easa, M. Atilhan, Viscosity and density of ternary solution of calcium chloride
910 + sodium chloride + water from T = (293.15 to 323.15) K, J. Chem. Eng. Data. 59 (2014) 2133–2143.
911 https://doi.org/10.1021/je500070k.

912 [70] B. Liu, B.S. Mahmood, E. Mohammadian, A.K. Manshad, N.R. Rosli, M. Ostadhassan, Measurement of
913 solubility of CO2 in NaCl, CaCl2, MgCl2 and MgCl2 + CaCl2 brines at temperatures from 298 to 373 K and
914 pressures up to 20 mpa using the potentiometric titration method, Energies. 14 (2021).
915 https://doi.org/10.3390/en14217222.

916 [71] M. Sorai, T. Ohsumi, M. Ishikawa, K. Tsukamoto, Feldspar dissolution rates measured using phase-shift
917 interferometry: Implications to CO2 underground sequestration, Appl. Geochemistry. 22 (2007) 2795–2809.
918 https://doi.org/10.1016/j.apgeochem.2007.06.019.

919 [72] P. Ranganathan, R. Farajzadeh, H. Bruining, P.L.J.J. Zitha, Numerical Simulation of Natural Convection in
920 Heterogeneous Porous media for CO2 Geological Storage, Transp. Porous Media. 95 (2012) 25–54.
921 https://doi.org/10.1007/s11242-012-0031-z.

922 [73] A. Jafari, T. Babadagli, Effective fracture network permeability of geothermal reservoirs, Geothermics. 40
923 (2011) 25–38. https://doi.org/10.1016/j.geothermics.2010.10.003.

924 [74] R. March, F. Doster, S. Geiger, Assessment of CO2 Storage Potential in Naturally Fractured Reservoirs With
925 Dual-Porosity Models, Water Resour. Res. 54 (2018) 1650–1668. https://doi.org/10.1002/2017WR022159.

926 [75] H. Vosper, K. Kirk, C. Rochelle, D. Noy, A. Chadwick, Does numerical modelling of the onset of dissolution-

convection reliably reproduce this key stabilization process in CO2 Storage?, Energy Procedia. 63 (2014) 5341–5348. https://doi.org/10.1016/j.egypro.2014.11.566.